Received: 21 June 2020 | Revised: 20 August 2022 | Accepted: 24 August 2022

DOI: 10.1002/dep2.207

The Depositional Record
Open Access
A journal of the International Association of Sedimentologists
WILEY

ORIGINAL RESEARCH ARTICLE

An exceptional sedimentary record of initial rifting on the East African Plateau in the Miocene: Lessons from depositional cyclicity and palaeoenvironmental proxies

Jens Hornung[1] | **Matthias Hinderer**[1] | **Dennis Brüsch**[1] | **Rainer Petschick**[2]

[1]Institut für Angewandte Geowissenschaften, Technische Universität Darmstadt, Darmstadt, Germany

[2]Institut für Geowissenschaften, Goethe University Frankfurt am Main, Frankfurt am Main, Germany

Correspondence
Jens Hornung, Institut für Angewandte Geowissenschaften, Technische Universität Darmstadt, Schnittspahnstrasse 9, 64287 Darmstadt, Germany.
Email: hornung@geo.tu-darmstadt.de

Funding information
Deutsche Forschungsgemeinschaft, Grant/Award Number: HI643/7-2

Abstract

Knowledge about the initial tectonic and depositional dynamics, as well as the influence of early rifting on climate and environmental evolution remains speculative to a large extent, because sediments are usually deeply buried. Within the East African Rift System, inversion tectonics uplifted a few of these successions to the surface hence presenting rare windows into the pre-rift depositional history. One such example, an exceptional 700 m long and up to 60 m high fresh road cut provided the opportunity to study in detail initial rift successions of the southern Albertine Rift (Western Uganda). This focusses on the basal and poorly known Middle to Late Miocene in order to unravel the climatic, environmental, hydrological and tectonic evolution of the initial Albertine Rift. A large and robust multi-proxy dataset was gathered comprising 169 m of stratigraphic thickness, which spans from 14.5 to 4.9 Ma according to a revised lithostratigraphic model. Fieldwork comprised logging of the sedimentary record, spectral gamma ray, magnetic susceptibility and 2D wall mapping with photomosaics. Additionally, the sections were sampled for bulk mineral and clay mineral analysis. The succession exposes a suite of lithofacies and architectural elements detailing the evolution of a fluvio-lacustrine system. Five depositional environments were identified which show an overall back-stepping trend from an alluvial plain to a delta plain and finally palustrine/shallow lacustrine conditions. Mesoscale base-level cycles, preservation potential of architectural elements, and stacking pattern exhibit limited accommodation space. However, it increases over time. This overall trend indicates increasing tectonic subsidence, which can be explained by flexural downwarp within the pre-rift phase and in the upper part grading into fault-controlled crustal extension of the syn-rift phase, which more and more disrupted a large-scale river system. From the Middle Miocene up to the early Pliocene, this study revealed that palaeoclimate trends become marked by increasing and more fluctuating Th concentrations, loss of feldspar, intercalated lenses of hydroxosulphate minerals, and a shift from smectite-dominated to kaolinite-dominated clays. These signals are all interpreted as detrital except for the hydroxosulphates,

and they mirror the increasing intensity of chemical weathering and stripping of soils in the catchment. A trend towards increasing humidity is supported by an increase in lacustrine sediment facies and a lake-level rise. Nevertheless, intercalation of hydroxosulphate, ferricretes and pedogenised horizons prove ongoing seasonality and dry intervals. Finally, based on a revised stratigraphic model a sequence stratigraphic correlation of the outcrop's depositional cycles with basin-scale cycles is presented. According to these cycles, transition from the pre-rift to the syn-rift stage is marked by an unconformity and a tectonic pulse in the latest Miocene. However, the response of fluvial supply, the depositional system as well as climate conditions are less punctuated and characterised by gradual trends and temporal delays. The long pre-rift phase (*ca* 10 Myr) and the gradual transition to the syn-rift phase is in accordance with the active rifting model, which is based on thermal thinning of the lithosphere by asthenospheric upwelling.

KEYWORDS

Albertine rift, base-level, clay mineralogy, depositional cyclicity, EARS, gamma-ray, hydroxosulphate, magnetic susceptibility, palaeoclimate, sedimentology, sequence stratigraphy, thorium

1 | INTRODUCTION

Geological investigations of initial rift stages often suffer from a lack of data due to deep burial of strata in later rift stages and/or incomplete well data (no coring, etc.). However, subsidence, sediment flux and environmental data from the onset of rifting has a crucial impact on our understanding of how river systems, environments and the depositional record evolves during later rift stages, because principal depositional and tectonic patterns are frequently inherited (Talbot & Williams, 2009).

Continental rifts are extension features on rigid continental platforms, which develop as active rifts either by asthenospheric upwelling or as passive rifts via far-field-driven extension (Ebinger et al., 2002; Turcotte & Emerman, 1983). The distinction of these two types of rift evolution is based on the initiating process of lithospheric extension, but becomes less clear during their evolution when active and passive forcing appear to interact (Merle, 2011). Ebinger et al. (2002) points out that the result of active and passive rifting can produce similar rift structures and that rheologic properties of the crust play an important role. The initial phase of the active and passive type of rifting, however, produces different pattern of lithospheric stretching, magmatism and subsidence both operating on different time scales. Active rifting is initiated by asthenospheric upwelling and usually linked to a mantle plume. At the beginning, this leads to large-scale updoming [regional asthenosphere uplift], often accompanied by extensive volcanism. In a second stage, ongoing lithospheric thinning leads to downwarping and diffuse rifts, before distinct narrow rifts are formed. For active rifting, the entire process of thermal thinning and stretching of the lithosphere may last several tens of millions of years (Cloetingh & Ziegler, 2009; Turcotte & Emerman, 1983). Passive rifting is related to direct rupturing of the crust and suggests a relatively rapid formation of distinct rifts by pure shear or simple shear extension (Cloetingh & Ziegler, 2009). In this case, the asthenosphere is passively upwelling and rift magmatism succeeds rift formation.

The most prominent example of active rifting in younger Earth history is provided by the East African Rift System (EARS). Marine records suggest that updoming and regional scale uplift began in the late Eocene to early Oligocene in Ethiopia and initiated a first rifting episode (EARS 1 according to Macgregor, 2015). Before 20 Ma updoming moved farther south (EARS 2 according to Macgregor, 2015) most probably because of motion of the African Plate and created the Kenya Dome (Chorowicz, 2005; Guillocheau et al., 2018). Rift formation in the northern Kenya region started in the mid-Miocene and prograded to the south along a western and an eastern branch. Whereas the eastern branch is associated with intense magmatism, it is absent or minor in the western branch. The most voluminous volcanic centre in the western branch, the Virunga province, started at 12.3 Ma (Chorowicz, 2005). Although the active rifting model basically suits to the initiation of the EARS, its evolution and structure is strongly controlled by lithospheric-scale pre-existing weaknesses (Chorowicz, 2005; Ebinger, 1989; Ebinger et al., 2002; Macgregor, 2015). Obviously, the EARS avoids Archaean cratons and follows the frame of

the N-striking Mozambique belts that affected Eastern Africa during the Pan-African events at the end of the Neoproterozoic (Chorowicz, 2005). Moreover, the modern stress field implies a passive component of rifting. Stamps et al. (2008) could show that GPS data and earthquake slip vectors are consistent with 3.2 Myr-average spreading rates and transform-fault azimuths along the South-west Indian Ridge thus implying a far-field strain component in the Pliocene to recent EARS.

The motivation for this study was provided by an exceptional large road cut (700 m wide, 169 m of stratigraphic thickness) penetrating through all Miocene formations in the southern Albertine Rift. It belongs to the western rift branch of EARS 2 according to Macgregor (2015) and was studied immediately after exposure in 2012. The new outcrop provided a unique view into the initial stage of the Albertine Rift and related depositional processes, which may be a reference for the initial phases of other segments of the EARS and a useful case study also for other active rifts. The excellent outcrop enabled a comprehensive outcrop analogue study combining field observations and measurements including 2D wall-panels, sediment logs, spectral gamma ray logs and magnetic susceptibility logs, together with fresh sediment sampling and the application of a wide set of mineralogical and geochemical methods without facing major problems due to tropical in-situ alteration. To determine the provenance of the sediments. Schneider (2019) and Schneider et al. (2016a, 2016b) already published a part of the petrographical and mineralogical data of this outcrop such as bulk mineral analysis, heavy mineral analysis, bulk geochemistry and single grain analysis. Here clay mineral analysis is added to account for the weathering regime and early diagenesis. The data are merged to answer the following questions: (i) Do the depositional processes confirm smooth subsidence as expected from active rifting? (ii) How is ongoing rifting reflected in the evolution of depositional successions? (iii) How can initial rifting be linked to trends in palaeoenvironment and palaeoclimate as derived from different proxies.

2 | GEOLOGICAL SETTING AND STUDY AREA

2.1 | The Albertine rift

The EARS stretch over 6000 km and crosses all tropical climate zones (Figure 1; Chorowicz, 2005). In its centre, it developed two highly segmented branches: the eastern and the western branch (Macgregor, 2015). Along

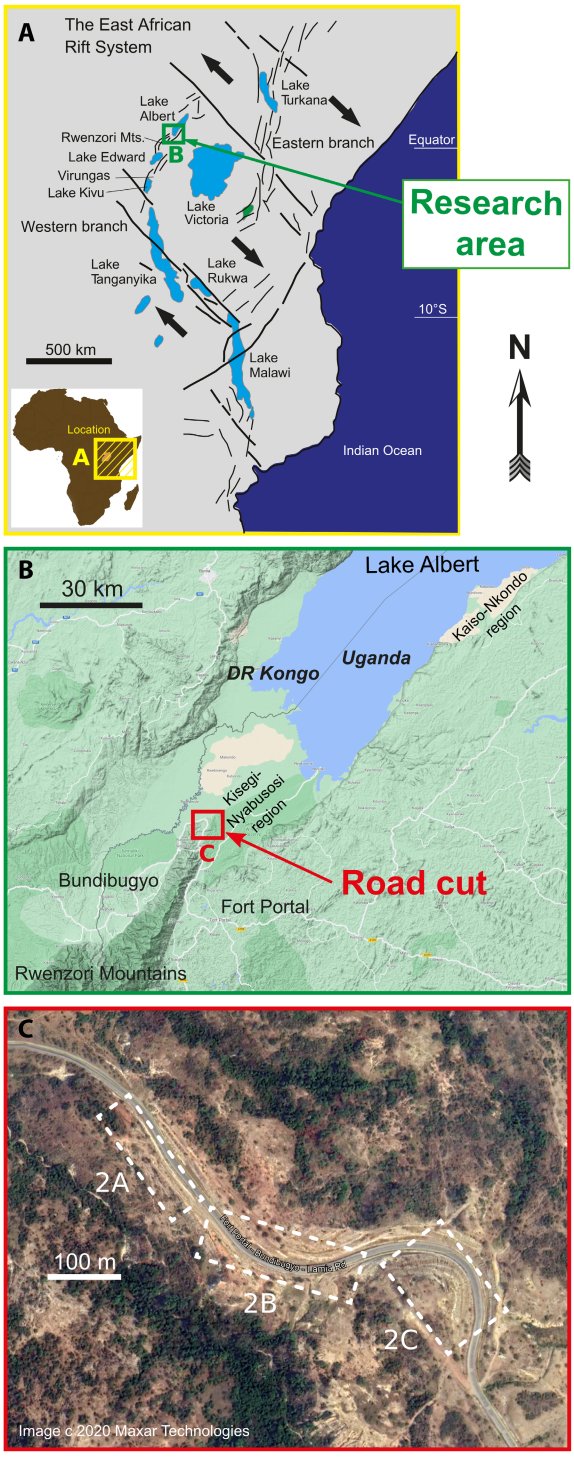

FIGURE 1 (A) Large-scale tectonic setting of the East African rift system based on Rosendahl et al. (1992). Green box (B) indicates zoom-frame of the research area. (B) Location of the investigated road cut with its position at the northern tip of the Rwenzori Mountains and the Albert rift. Coordinates are N 00.91855 and E 030.24454. Figure compiled from Google maps. (C) Satellite image showing the road cut in 2020. Dotted boxes indicate the area shown in the outcrop panels of corresponding Figure 2A–C. Figure compiled from Google Earth.

the length of the rift, en echelon border-fault segments linked by oblique-slip transfer faults created numerous mostly isolated and asymmetric rift basins bordered by high-angle normal faults (Ebinger, 1989). These individual rift basins were successively filled with fluvial to lacustrine sediments, which record the tectonics and climate of rift evolution during the Miocene based on the interaction of subsidence and sediment supply (Hinderer & Einsele, 2002). They bear the most important archive of palaeoenvironment and palaeoclimate in the interior of Africa since the Oligocene (Chorowicz, 2005).

Only a few localities within the EARS provide exposed Miocene sediments on hanging wall blocks within the rift. These are (i) the Ngorora Formation in Kenya (Upper to Middle Miocene; Rasmussen et al., 2017), along the east and west sides of Lake Turkana (Feibel, 2011), (ii) Upper Miocene deposits in the Middle Awash valley (Ethiopia; WoldeGabriel et al., 2000), (iii) in the Rukwa Rift of Malawi (Mtelela et al., 2017) and (iv) Middle to Upper Miocene deposits in the Albertine Rift (Lukaye et al., 2016; Pickford et al., 1993; Simon et al., 2017). The investigated outcrop belongs to the Middle Miocene to lower Pliocene. Summarised in the following are the main sedimentological and stratigraphic studies dedicated to the corresponding rift segment so far.

The sediment succession of the Albertine Rift can be mainly studied in two regions offshore of Lake Albert: (i) the Kisegi–Nyabusosi area in the south and the (ii) Kaiso–Nkondo area at the foot of the eastern graben shoulder (Figure 1). The Kisegi–Nyabusosi area in the southern Albertine Rift is the only place where sediments are exposed recording all stages of rift evolution. Sediments overlying the crystalline basement reach a thickness of 600 m (Pickford et al., 1993), which is much lower compared to the same stratigraphic interval in the central rift, where 5000 m thickness are found in seismic data (Simon et al., 2017). The Kisegi–Nyabusosi area has been mapped and biostratigraphically investigated since the 1960s (for review see Pickford et al., 1993). Pickford et al. (1993) and Van Damme and Pickford (2003) subdivided the sedimentary record of the Kisegi–Nyabusosi region into eight formations and published a geological map for this region. Pickford's stratigraphy is based on freshwater mollusc associations dating back to the Middle Miocene. The dating and time-span of these mollusc assemblage zones are confirmed and slightly modified by correlation with tephrostratigraphic data of the Kenia-Rift (Simon et al., 2017). Roller et al. (2010) correlated 19 sedimentary sections to this biostratigraphic framework. These outcrops were located 0.3 km west to 4.6 km southeast around the road cut and show similarity in terms of sediment facies and overall stratigraphic trends. However, because of fluvial self-organisation, which does not allow sustainable beds and a very high soil cover correlation of these outcrops at bed or even architectural element scale is not possible. Lateral trends towards more basinward or landward positions of deposition are not recognised within these few kilometres.

Simon (2015) and Simon et al. (2017) complemented the existing offshore data with an exceptional subsurface data set including 2D seismic reflection surveys and data from seven exploratory wells. Together with a re-evaluation of the outcropping data, they reconstructed the tectonosedimentary evolution of the Albertine Rift. Revision of the biostratigraphy of Pickford et al. (1993) extended the time scale for the oldest sediments in the Albertine Rift to 17 Myr (Simon et al., 2017). They could distinguish three main evolutionary stages for the Albertine Rift:

(i) Pre-Rift phase from 17.0 ± 0.8 Ma to 6.2 ± 0.2 Ma with low and diffuse deformation.
(ii) Rifting phase 1 from 6.2 ± 0.2 Ma to 2.7 ± 0.2 Ma with strong, fault-controlled subsidence.
(iii) Rifting phase 2 from 2.7 ± 0.2 Ma to present-day with lower subsidence in sub-basins, scarp uplift and drainage inversion phase.

Schneider et al. (2016a, 2017) carried out provenance analysis of rift sediments at outcrops in the Kisegi–Nyabusosi and the Kaiso–Nkondo area. From petrography, heavy mineral suits, and single grain analysis of rutile and garnet they could identify two changes of provenance: a first one around the Miocene/Pliocene boundary at *ca* 5.5 Ma, and a second one around the Pliocene/Pleistocene boundary at *ca* 2.5 Ma. The timing is well in accordance with the three-stage tectonosedimentary model of Simon et al. (2017). The somewhat younger ages can be interpreted as a delayed response and time for reorganisation of the drainage system to tectonic rifting activity. Moreover, the provenance data point to a large-scale drainage system over east Africa in the Miocene, that is, in the pre-rift phase. Such a continent-wide, west-directed drainage system to the Atlantic Ocean was postulated already in the 1950s (de Heinzelin, 1959). Most probably, this drainage system had its headwaters in the mountains of the Pan-African Orogen to the east (Mozambique Belt). Gagnevin et al. (2017) could confirm this through U–Pb zircon chronology, and Pb isotopic analysis of K-feldspar from well samples in the northern Albertine Rift. Based on this geochronology the distance of sediment transport can be constrained to more than 500 km during the

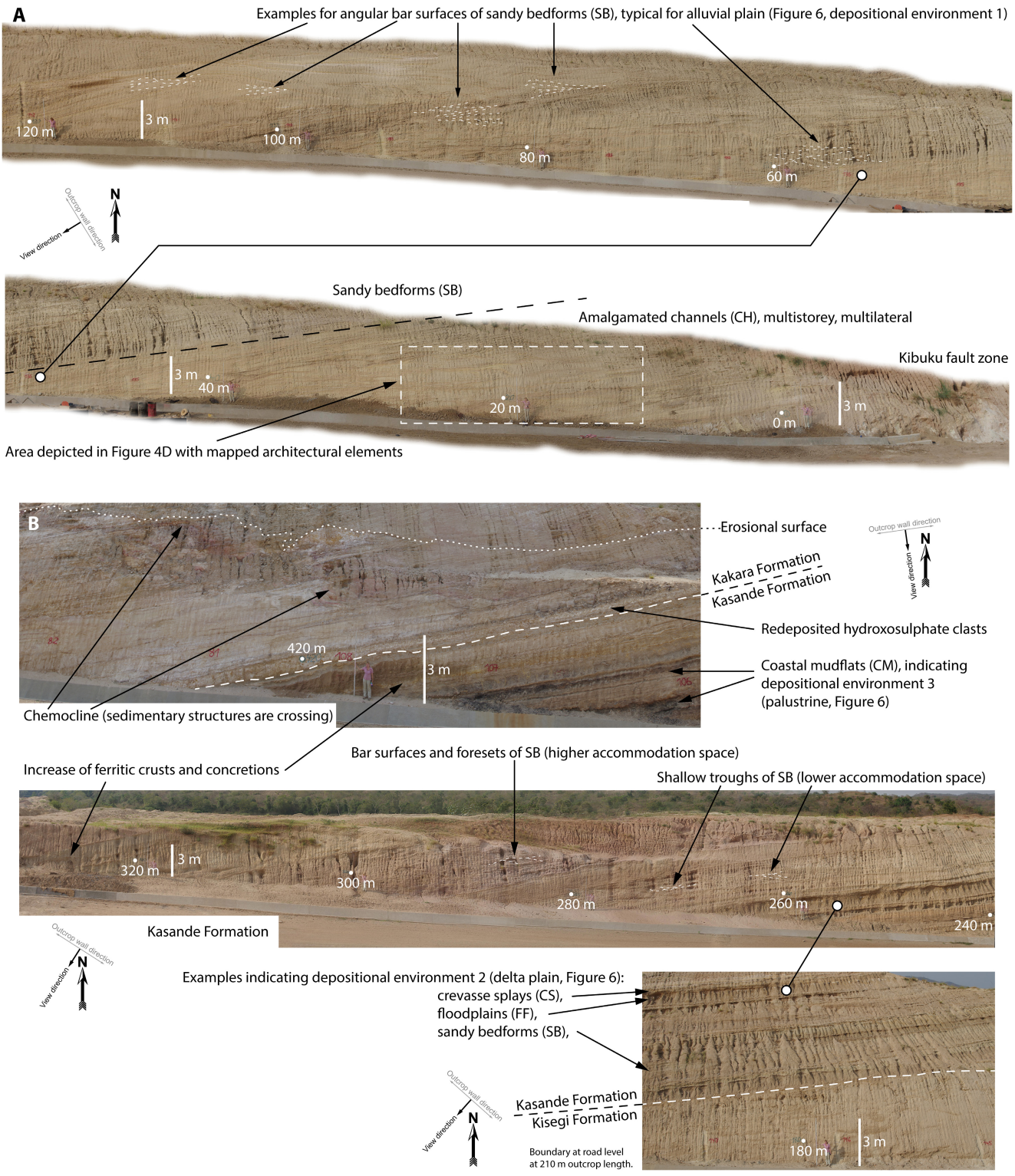

FIGURE 2 Legend on next page

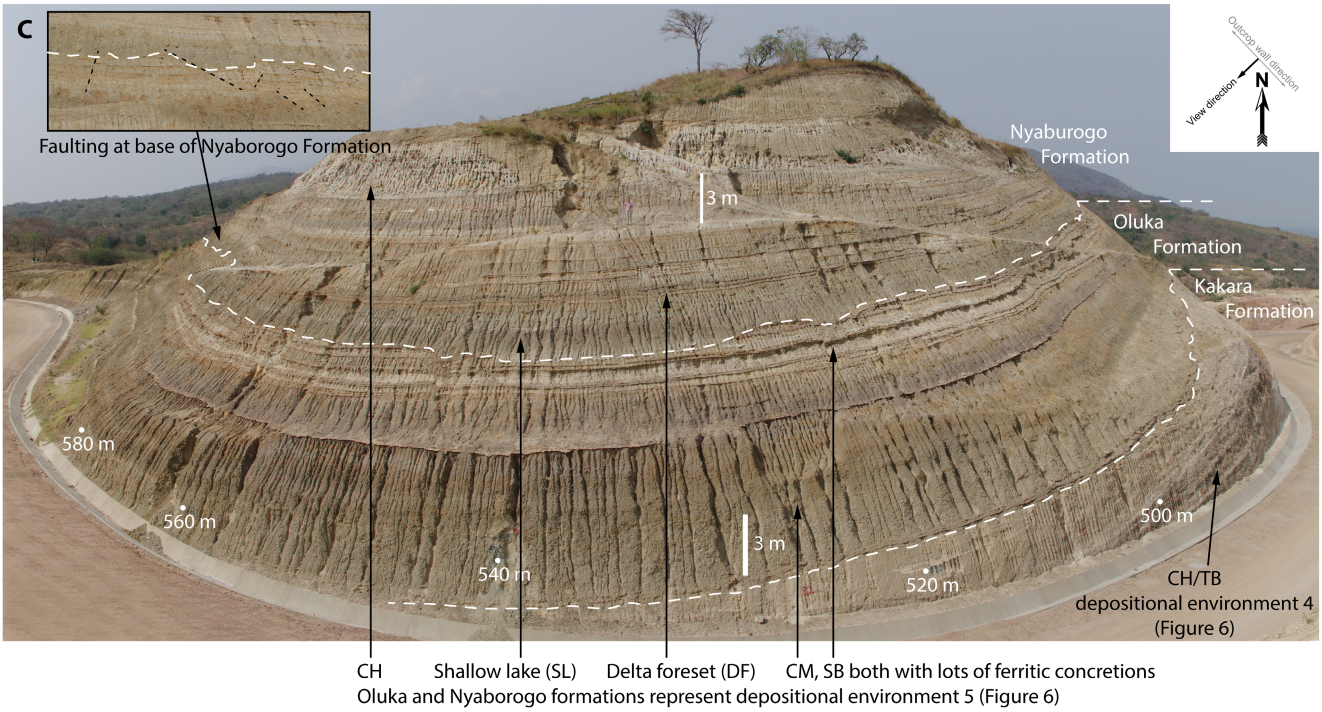

FIGURE 2 (A) Merged photopanel of the lowermost part of the outcrop wall. Exposed is the Kisegi Formation. Note the braid-plain character with highly amalgamated channels (CH) and dominance of sandy bedforms (SB) indicating a fluvial bedload environment. Stacking patterns are multilateral and multistorey. (B) Lower right: The boundary of the Kisegi to Kasande formations according to Lukaye et al. (2016) is marked with a white dotted line. It is located where the first crevasse splays (CS) and floodplains (FF) are preserved. Centre: Merged photopanel of the Kasande Formation as exposed in the middle part of the outcrop wall showing typical brownish-yellowish beds and clay rich intervals. Stacking is sheet-like, aggradational, and beds often show an erosional base. In its lower part, the Kasande Formation shows frequent coarsening upward sand beds dedicated to delta front lobes. Upper left: In the upper part of the Kasande Formation occur coastal shoal deposits (CM) and channels of the lower delta plain. White dotted line depicts the boundary of Kasande to Kakara formations according to Lukaye et al. (2016). It is located shortly above the two dark grey organic-rich clay beds (CM) and below hydroxosulphate clasts. Please note a complex erosional surface in the Kakara Formation showing prominent downcutting and suspected to represent the 'S3Un' basin-wide traceable unconformity of Simon et al. (2017). Chemocline colours imitate boundaries, but sedimentary structures are persistent. The outcrop continues for 240 m to the right (north-west) as indicated by distance marks and another 380 m to the left (south-east) (C) Merged photopanel of the uppermost part of the outcrop. Exposed are the Nyaburogo, Oluka, and the uppermost part of the Kakara formations. Boundaries according to Lukaye et al. (2016) are marked with white dotted lines. White dots with metres show the distance to the lower end of the road cut (north-west, to the right). Total length of outcrop is 700 m. Due to optical distortion, an overall scale cannot be provided, but scale bars and distance marks allow estimates for non-linear scaling. Note the erosional character of some beds showing downcutting and synsedimentary tectonics in the upper part of the Oluka Formation (e.g. detail photograph in upper left corner).

Miocene. Provenance change at the Miocene/Pliocene boundary point to a shift of sediment supply to more local sources. This fits into the tectono-sedimentary model, which states a shift from diffuse extension with moderate subsidence to accelerated, largely fault-controlled subsidence. Most probably, this disrupted the large-scale drainage system and led to a segmentation into small-scale drainage basins (Schneider et al., 2016a, 2017). Hence, the Albertine Rift provides an excellent example for the depositional response at the transition from the pre-rift to the syn-rift phase, yet while the depositional environments are anticipated to transition from fluvial to lacustrine (Chorowicz, 2005), there has not been a detailed study thus far.

2.2 | The road cut in the Kisegi–Nyabusosi area

The outcrop is located at N: 00.91855 and E: 030.24454 and exposes a sediment succession of 169 m stratigraphic thickness and a lateral extent of *ca* 700 m, studied shortly after excavation (January 2012). Stratigraphic correlation of the road cut to those of Roller et al. (2010) and Simon et al. (2017)

is entirely based on lithological criteria according to descriptions of Pickford et al. (1993), Roller et al. (2010), National Stratigraphic Commission of Uganda (2011), and Lukaye et al. (2016). Lukaye et al. (2016) states that the topmost part of the outcrop already corresponds to the Nyaburogo Formation, which would mean that the succession comprises five of the eight formations in the Kisegi–Nyabusosi area: Kisegi (Figure 2), Kasande, Kakara (Figure 2B,C), Oluka and Nyaburogo (Figure 2C) formations ranging from *ca* 17 to <4.9 Ma according to biostratigraphy. This corresponds to a time-span of *ca* 12 Myr and a Middle Miocene to earliest Pliocene age. Tectonically, the road cut section belongs to a fault block, framed by the Rwenzori Fault in the west and the Tonya Fault in the east. Within the road cut, faults are absent, except for one major regional fault zone (Kibuku Fault) in the lower part, represented by two shear zones, which are synsedimentary and limited to a throw of less than a few metres, thus, sedimentary correlations are not hindered. The basin-wide traceable unconformity at 6.2 Ma described by Simon et al. (2017) is within the exposed stratigraphy. Frequently, there occur further erosional surfaces with significant downcutting.

3 | MATERIAL AND METHODS

3.1 | Sedimentological logging

The entire 169 m thick stratigraphic succession was logged using a lithofacies and an architectural element catalogue following Miall (1996, 2016) and Hornung and Hinderer (2011). Lithofacies distribution is sensitive to short-term depositional energy, whereas architectural element distribution provides information about long-term depositional energy and about depositional environments and fluvial styles. Resolution of sedimentary logging followed a nested approach, which means thick uniform units were measured at decimetre scale and thin beds at centimetre scale. This ensures that short excursions in the depositional record are also represented in the dataset. The distribution of the architectural elements and stacking patterns was analysed with the help of 2D photomosaics. A high-resolution camera moving along the outcrop with an image overlap of 50% and mounting the individual shots later with Photomerge stitching software from Adobe Photoshop™ created the photomosaics.

3.2 | Cycle analysis and sequence stratigraphic background

Depositional cycles were established based on the stratigraphic base-level approach of Cross et al. (1993) and Ramón and Cross (1997) and which are also partly discussed in Catuneanu et al. (2009). Stratigraphic base-level cycles were defined by trends of an increasing or decreasing ratio of accommodation space (A) to sediment supply (S), which is d/dt(A/S). A lack of accommodation space and/or high sediment supply corresponds with high stream power (=depositional energy) and vice versa. Using the experiments of Reineck and Singh (1980) and observations of Stow et al. (2009), lithofacies types can be interpreted in terms of these depositional energy levels. Applying this, in times of low accommodation space and high sediment supply (low base-level) only high-energy lithofacies types are preserved, such as lag-deposits, coarser grain sizes and cross-beds. Low-energy lithofacies types such as clay and plane bedded or rippled silt are preferentially preserved during times of high accommodation space and low sediment supply (high base-level).

Architectural elements and their stacking patterns reveal information about preservation potential from which trends in accommodation space and stratigraphic base-level can be interpreted (Cross et al., 1993; Hornung et al., 2020). Decreasing accommodation space and/or increasing sediment supply triggers sediment bodies and facies zones to prograde towards the basin centre producing progradational stacking patterns in the depositional record. Hence, progradation is tied to the base-level fall hemicycle. During times of low accommodation, only high-energy architectural elements such as scour fills, channel lags, gravel bars and sandy bedforms of channel bases can be preserved. Erosion occurs in times of negative accommodation space.

Low-energy architectural elements such as levees, floodplains and coastal mudflats or lake deposits are preferentially preserved in times of highly available accommodation space and low sediment supply (high base-level). Increasing accommodation space or decreasing sediment supply induce sediment bodies and facies zones to retrograde towards the basin margin producing retrogradational stacking patterns in the depositional record. The retrogradational trend corresponds to base-level rise hemicycle. A full cycle comprises both, a fall and a rise hemicycle.

During a stratigraphic base-level fall hemicycle, accommodation space is limited. Hence, superpositioned lower-order fall hemicycles can hardly be preserved as accommodation space becomes even rarer. However, when a lower-order rise hemicycle is superposed on this higher-order fall hemicycle, it contributes to more accommodation space. Hence, preservation potential becomes higher and the superposed rise cycle can be preserved (Figure 3). Preferential preservation of rise hemicycles is typical for proximal or medial positions [related to source region] in a sediment routing system, where deposition is mainly accommodation space controlled, because supply is permanently available due to the close proximity of the source region.

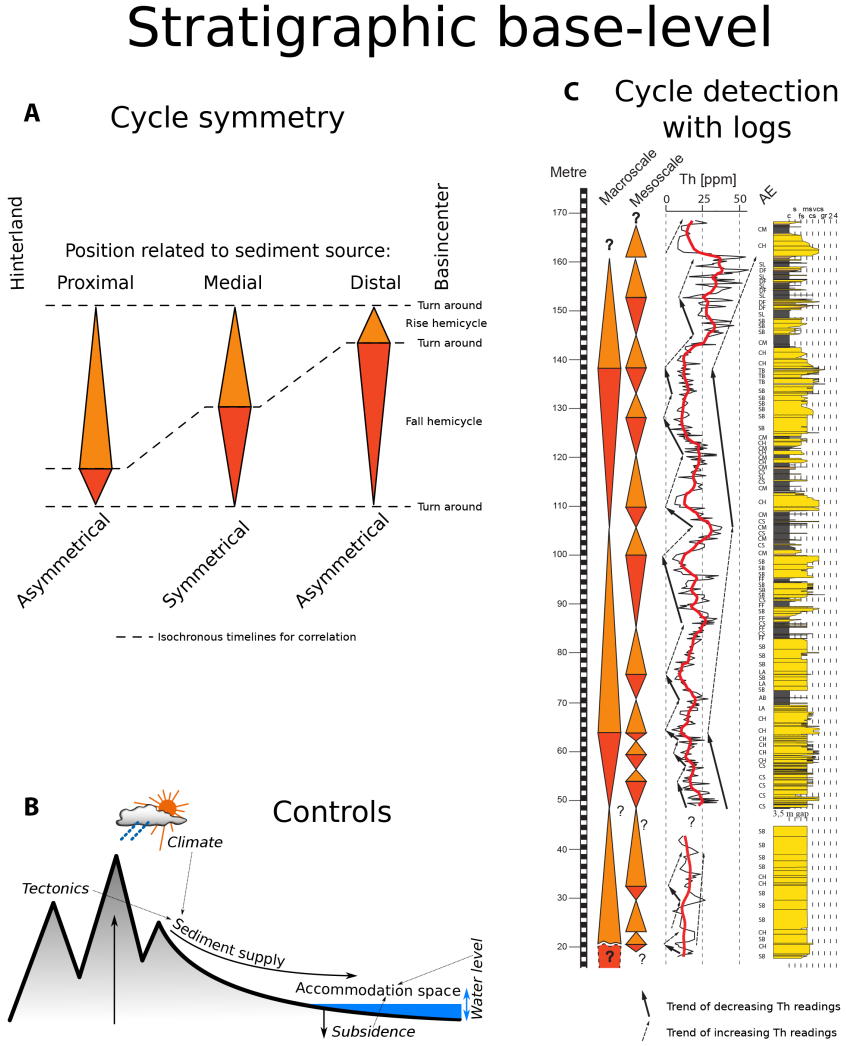

FIGURE 3 (A) Cycle symmetry: Symmetry of stratigraphic base-level cycles changes systematically along a sediment routing system. The turn-around points of hemicycles represent isochronous timelines, as they are governed by regional controls. (B) Controls: For stratigraphic base-level, timely changes of these main controls are crucial. without change, the disequilibrium between accommodation space (A) and sediment supply (S) will be rapidly balanced and deposition would stop. This can be expressed by d/dt(A/S). (C) Cycle detection: Two hierarchies of stratigraphic base-level cycles (triangles) are found. Note the systematic change in symmetry relationships along stratigraphy at both scales. Thorium log (thin black line) with overlaid Gaussian filter (red line). Increasing trends of thorium readings are highlighted with thin dotted arrows, decreasing trends in thorium log with thick solid arrows. Increasing values support stratigraphic base-level rise hemicycles and decreasing ones fall hemicycles. Sedimentary section shows that these trends perfectly mirror the depositional cycles represented in the sedimentary record and coincides with depositional energy and preservation potential. For details, see background section in the text.

In the other case, during a higher-order rise hemicycle, the highly available accommodation space would also allow preservation of a superposed fall hemicycle. In this situation, everything can be preserved, lower-order rise and fall hemicycles. Usually, this occurs in distal positions when accommodation space overwhelms sediment supply leading finally to lake deposits (in overfilled basins). In such distal positions, deposition only takes place when sediment supply happens, preferentially leaving base-level fall hemicycles in the depositional record. Hence, the system is supply controlled.

Changes in preservation potential during higher-order base-level cycles or differences in the position within the sediment routing system lead to different thicknesses of rise and fall hemicycles. If the thickness of both hemicycles is equal, the full cycle will be symmetric. Asymmetry occurs when the thickness of the hemicycles is different (Figure 3A).

Stratigraphic base-level cycles are governed by allogenetic regional controls, such as tectonics, subsidence, sea or lake level and climate (Figure 3B). Subsidence and water level fluctuations are mainly responsible for accommodation space creation, whereas tectonic uplift and climate contribute dominantly to sediment supply. Tectonic control is typically reflected by higher-order cycles, that is, macrocycles are expected here to largely record tectonic movements of initial rifting.

Hence, changes in trends towards rising or falling A/S ratio (stratigraphic base-level) lead to formation of regional stratigraphic surfaces (Catuneanu et al., 2009). These surfaces are called turn-around points and can be used to correlate completely different facies successions (facies belts, facies zones) isochronously in a basin-wide context by establishing timelines between these turn-around points (Figure 3A, Cross & Lessenger, 1998).

Beside the A/S ratio, the depositional cycles and turn-around points are detected within this work using the shape and behaviour of spectral gamma ray logs. As an example, Figure 3C illustrates how Th concentration supports stratigraphic base-level cycles. A base-level fall features a decrease in Th concentrations and vice versa. For reasons, see Results and Discussion chapters.

3.3 | Spectral gamma ray logging

Natural spectral gamma radiation reveals total concentrations of K, U and Th. Four hundred and seventy one measurements were distributed following the same nested approach as sedimentological logging to ensure that all beds were accounted for. A hand held device from Exploranium Ltd. (GR 130) was used which has a 2.5″ NaJ-Detector with subsequent photomultiplier. Peak stabilisation for correct channel assignment was performed within 2–4 h using a 137 Cs source. Because radioactive decay is an erratic process, a sufficient integration time is needed to produce a stable average of the readings. Therefore, a time series measurement was performed up to 600 s, which showed that from 100 s onward data became stable. Only data under 60s become detrimentally unstable (Hornung & Hinderer, 2011). Prior to and after outcrop measurements, a daily test measurement on air and on a standard rock was performed to get background radiation and to monitor possible sensor drifts. During the day and over the time-span of the whole measuring campaign no changes were recognised, hence, no corrections were required. Due to small-scale changes in lithology, a significant scatter was observed in the readings. Hence, for better recognition of general trends a Gaussian filter was applied to slightly smooth the logs, which is displayed as an overlaid graph (see Figure 3C and Section 4.4).

3.4 | Magnetic susceptibility

The magnetic susceptibility of a sediment is a function of the magnetic properties of the constituent minerals (dia-, para-, canted antiferro-, ferri- and ferromagnetic sensu *lato*) and of their spontaneous magnetisation, grain size, internal stress and other non-intrinsic parameters (Thompson et al., 1975). The 950 magnetic susceptibility measurements were carried out with the magnetic susceptibility meter SM-30 from GF Instruments. A 5×8 cm large, sub-vertical area was flattened to allow the device to be in contact with the sediment. A close spacing in decimetre to sub-decimetre scale was applied following again the nested approach to account for each bed. Each value is corrected for drift and background radiation of the environment by a triple measurement air-rock-air. In order to visualise general trends, data were smoothed with an overlaid Gaussian filter, which makes it easier to recognise trends that underlie the scattering of readings.

3.5 | XRD measurements

Analyses were performed following the instructions by Moore and Reynolds (1997). In total 33 preparations were made. Eighteen sediment samples and seven hydroxosulphate beds use oriented powder preparations as evaporated resuspensions of the clay-sized fraction on glass slides (about 4 mg/cm^2). Eight bulk-sediment analyses were carried out on powder specimens (=unoriented). The whole rock and clay mineral composition was analysed by a PANalytical X'pert PRO diffractometer (Cu-Kα radiation generated at 40 kV and 30 mA) at Goethe University in Frankfurt am Main (Germany), which is equipped with a variable divergence slit and an X'Celerator detector. The oriented specimens were scanned between 2° and 40° 2θ (air-dried specimens) or 2–22° 2θ (ethylene glycol solvated specimens) with a step size of <0.01° 2θ and a counting time of 10 s per step. The unoriented bulk-rock powder specimens were scanned between 2.5° and 90° 2θ and a counting time of 5 s per step. The mineral content in the bulk-rock samples was determined by intensities of the highest XRD maximum of each phase using the Reference Intensity Ratio (RIR). The RIR method normalises all diffraction data to a standard, which is by convention, corundum (ICCD-International centre for diffraction data, PDF-2). The analysis of XRD diagrams were implemented using the program MacDiff (Petschick, 2001). The terms smectite, illite and kaolinite are used here as a proxy for the particular mineral groups. The relative clay mineral contents (rel.%) were determined by using ratios of integrated peak regions of their basal reflections (Petschick et al., 1996) weighted by empirically estimated factors from Biscaye (1965).

4 | RESULTS AND INTERPRETATION

4.1 | Depositional dynamics and environments

Along the road cut, 11 sedimentary lithofacies types were identified and described (Table 1) based on their grain

TABLE 1 Lithofacies classification of recorded sediments in the Semliki road cut section following the approach and codes of Miall (1996, 2016) and Hornung and Hinderer (2011).

		Sedimentary inventory				Interpretation		
Code name	**Bedding**	**Fabric**	**Dominant grain size**	**Sorting**	**Size (m), Laterally vertically**	**Hydrodynamic**	**Genetic**	**Depositional energy level**
Gmg **G**ravel **m**assive **g**rain supported		• Structureless • Chaotic texture • No trends • Contains lithoclasts	Ms-gr (3 cm)	Very poor	>30 0.5	Rapid deposition and short distance bed load transport does not allow for sorting or creating structures	In scour fills At channel bases In gravel bars (Miall, 1985)	Very high
Gpg **G**ravel **p**lanar **g**rain supported		• Planar cross-bedded • Dip angle 30–50° • Set thickness 35–40 cm • Contains lithoclasts	Fs-gr (2 cm)	Very poor	>30 0.4	Downstream-shedding of bed load over slope creates foresets	Migration of isolated, straight-crested transverse bedforms or mid-channel bars Miall (1985); Hein and Walker (1977)	Very high
St **S**and **t**rough cross-bedded		• Trough cross-bedded • Foresets internally graded • Set thickness 5–45 cm • Contains extraclasts	fs-vcs, dominantly ms	Poor-well	>100 0.2–5	Eddies excavate troughs at luv-side between bedforms and shed material at lee-side. Transport as bed-load	Migrating subaqueous dunes with curved/sinuous crest Miall (1996); Allen (1984)	High
Sp **S**and **p**lanar cross-bedded		• Planar cross-bedded • Dip angle 30–50° • Topsets finer • Set thickness 3–150 cm • Can contain significant amounts of gr (2–3 cm)	ms Range fs-vcs	Very poor–moderate	>100 0.1–4	Bed-load and saltated material is shed down at lee-side of bedforms forming foresets	Migrating subaqueous ripples (<30 cm height) or lingoid or transverse bars (>30 cm height) with straight crests Miall (1996); Allen (1982)	Intermediate-low
Sr **S**and **r**ipple cross-bedded		• Trough and planar ripple cross-bedded • Set thickness 1–3 cm	fs-ms	Well	5 0.2–1	Bed-load and saltated material is shed down at lee-side of bedforms forming foresets	Migrating subaqueous small-scale ripples with straight or curved crests Nichols (2009); Allen (1982)	Low
Sm Sand massive		• Structureless • No trends	fs-vcs	Very poor-well	>50 0.05–1	Rapid deposition does not allow for creating structures	Gravity flows Falling stage deposits. Todd (1989); Miall (1996) Probably post-depositional destructuring like dewatering or bioturbation. Miall (1996)	High-intermediate
Sh **S**and **h**orizontally bedded	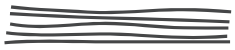	• Horizontally bedded	fs-ms	moderately-well	>10 0.15–0.2	Deposition under laminar flow conditions	Various	High or low

(Continues)

TABLE 1 (Continued)

Code name	Bedding	Sedimentary inventory			Size (m), Laterally vertically	Interpretation		
		Fabric	Dominant grain size	Sorting		Hydrodynamic	Genetic	Depositional energy level
Sl **S**and **l**ow-angle cross-bedded		• Low angle (<10°) bedded	fs-ms	Well	>5 0.2		In crevasse splays Miall (1985)	High
Fm **F**ines **m**assive		• Structureless • Silty claystones • Could contain significant Fe- and gypsum impregnations and bioturbation	s-c	Well	>100 0.01–2.4	Suspension fall-out in stagnant water areas	Littoral/marginal lacustrine Waning flood stage Overbank and drape deposits Miall (1977, 1996) Probably post-depositional destructuring like dewatering or bioturbation	Very low
Fl **F**ines **l**aminated		• Fine lamination • Laminae thickness mm- < cm • Silty claystones	s-c	Well	>100 0.35–1.5	Suspension fall-out in stagnant water areas	Lacustrine Waning flood stage Overbank deposits Miall (1977, 1985, 1996) Hyperpycnal Hornung and Aigner (1999) Probably post-depositional destructuring like dewatering or bioturbation	Very low
Fh **H**orizontally bedded		• Horizontally bedded • Set thickness cm-dm • Silty claystones	s-c	Well	>10 0.25	Suspension fall-out in stagnant water areas	Littoral/marginal lacustrine Waning flood stage Overbank deposits Miall (1985)	Very low

Note: Note that to preserve lithofacies types showing a high depositional energy level (right column) a high preservation potential is needed, which coincides with high accommodation space.

TABLE 2 Architectural element catalogue of the Semliki road cut section following the approach and codes of Miall (1996, 2016) and Hornung and Hinderer (2011). Right column provides a genetic interpretation, an estimation about depositional energy, and what relationship between accommodation space and sediment supply is indicated when the unit is preserved.

	Internal geometry			External geometry			Interpretation
Code (name), Appearance-sketch	**Masterbedding, Bed characterisation, Diagenetic features**	**Litho-facies make-up**	**Trends**	**Boundaries top contact bottom contact**	**Shape**	**Size (m), Laterally Vertically**	**Genetic interpretation, Depositional energy level, Indicator for accommodation space (A) and sediment supply (S)**
CH (**ch**annel) 	Trough, planar or dune shaped sandy sub-units as amalgamated bedforms (single storey) or channels stacked together as cut and fill (multi-storey)	St Sm Sp Sr Fm	Weak fining upwards	Mostly gradual Erosional	Trough	>30 1–4	Migrating and downcutting river beds in a highly dynamic channel-belt Very high depositional energy Low A; High S
SB (**s**andy **b**edforms) 	Planar, trough, massive to ripple bedded mostly medium to coarse grained sand Occur often as multistorey and multilateral stacked thicker units	St Sp Sm Fm	Coarsening and fining upward	Gradational Sharp Erosional Gradational	Tabular Lenticular Wedge	>200 0.2–4	Migratory bedforms, sand waves, linguoid and transverse bars within a sand dominated channel High depositional energy intermediate A, High S
LA (**l**ateral **a**ccretion) 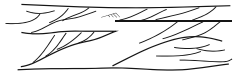	Planar to trough cross-bedded medium sand within commonly amalgamated accretion surfaces dipping 15–20°, set thickness 0.1–1 m. Heterolithic beds Often intensively ironhydroxide cemented horizons	Sp Sm Sr St Fm	Fining upward	Mostly gradational Erosional or gradational	Tabular to lenticular	>20 2	Channel migrates perpendicular to stream direction creating a cut bank and point bar deposits Intermediate depositional energy Both, A and S intermediate
AB (**ab**andoned channel) 	Thin horizontally bedded clay/silt beds interlaminated with thin massive sand packages (1–5 cm) Intensively interspersed by gypsum precipitations and initial soils/burrows	Fl Fm Sm	Fining upwards	Sharp Gradational	Trough	>100 3	Rapid abandonment of channels due to avulsion (lateral migration) or cut-off Low depositional energy High A; low S

(Continues)

TABLE 2 (Continued)

	Internal geometry			External geometry			Interpretation
Code (name), Appearance-sketch	**Masterbedding, Bed characterisation, Diagenetic features**	**Litho-facies make-up**	**Trends**	**Boundaries top contact bottom contact**	**Shape**	**Size (m), Laterally Vertically**	**Genetic interpretation, Depositional energy level, Indicator for accommodation space (A) and sediment supply (S)**
FF (**f**loodplain **f**ines) 	Massive to horizontally bedded clay/silt usually interbedded by CS Lots of carbonatic and ferrugenious nodules and concretions	Fm Fl	No trends	Sharp Sharp Gradational	Sheet Tabular	>100 0.2–1.5	Suspension fallout in flooded interchannel areas within the alluvial plain Very low depositional energy Very high A, very low S
CM (**c**oastal **m**udflat) 	Massive to horizontally bedded clay/silt alternating with thin sand packages. Rarely thin (~5 cm) organic rich layers Occasionally pedogenised, abundant gypsum and iron precipitation	Fm	No trends	Sharp Gradational Sharp	Sheet	>200 0.2–1.6	Mostly flooded lacustrine dominated delta plain interchannel area Very low depositional energy Very high A, very low S
TB (**t**ransverse **b**ars) 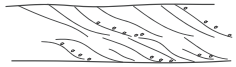	Planar cross-bedded medium sand to fine gravel. Accreting foresets dip at 15–20 ° angle	Sp Gpg Gmg	Overall thickening and coarsening upward	Erosional Erosional	Tabular sheet	>50 0.2–2	Fluvio-lacustrine interaction. Downcurrent accretion in a standing water body (lake estuarine/paralic) Low depositional energy High A, High S
DF (**d**elta **f**oresets) 	Massive to rarely ripple bedded thin and laterally persistent sand beds Intensively iron impregnated	Sm Sr	Coarsening upward	Sharp Sharp Rarely erosional	Tabular	<100 0.1–0.5	Bottom sets of prograding delta front Low depositional energy Very high A, low S
SL (**s**hallow **l**acustrine) 	Massive to horizontally bedded clay only minor silt fraction alternating with wavy 1–3 cm thick sand sheets Laterally persistent iron crusts, no gypsum precipitations	Fm Fh	No trends	Sharp Sharp Rarely gradual	Sheet	<200 0.5–1.5	Suspension fallout from water body Very low depositional energy Very high A, extremely low S

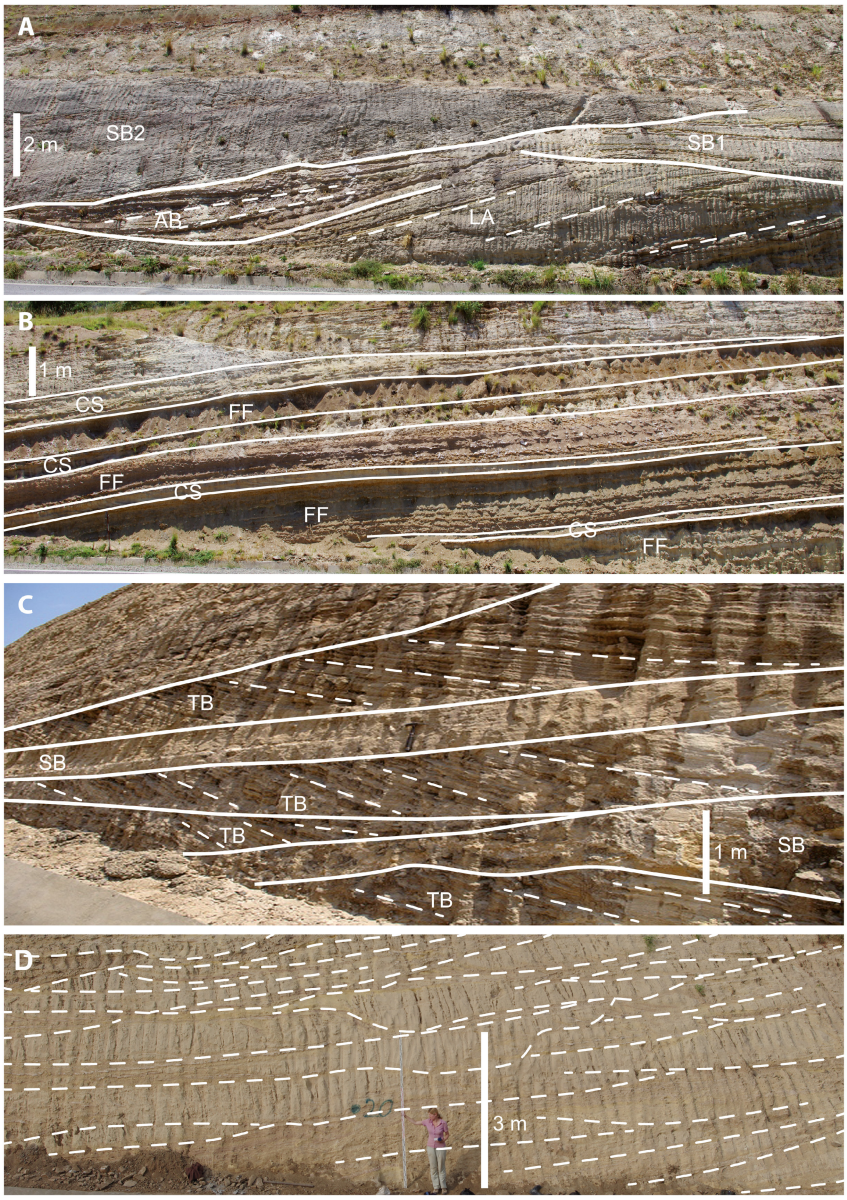

FIGURE 4 Examples for architectural elements representing different depositional environments in the road cut section. Thick solid lines display the boundaries of the architectural elements. Thin dotted lines represent internal bedding. (A) Heterolithic lateral accretion master bedding (LA) which transform into abandoned channel sediments (AB). The AB is reactivated from time to time, which is indicated by sandy bottom layers pinching out upwards along the masterbedding. The succession is overlain by two phases of amalgamated sandy bedforms (SB), which shed sand into the AB. The succession is typical for depositional environment 1 (see text). (B) Alternating succession of crevasse splays (CS) and flood plain fines (FF), diagnostic for depositional environment 2 (see text). (C) Large-scale, planar cross-bedded, and prograding transverse bar (TB) deposits, which corresponds to depositional environment 4 (see text). (D) Multistorey and multilaterally amalgamated fluvial channels (CH) indicating a braid plain environment represented at the basal part of depositional environment 1.

size, sedimentary structures, sorting and petrology. In addition, nine architectural elements are itemised and described in Table 2 and Figure 4, and an interpretation of preservation potential and available accommodation space is provided.

Based on Table 2, Figure 5 describes the sedimentary inventory of architectural elements along the log section. It interprets them in terms of five principal depositional environments, establishes associated log sections and interprets their preservation potential and availability of accommodation space. In addition, a position along the graded river profile is estimated to resolve progradational or retrogradational trends of facies zones. Chronological order is from depositional environment 1–5.

Depositional environment 1 (Figure 5): The log section 0–46 m shows fluvial channels (CH), channel lags and sandy bedforms (SB) as intensively amalgamated, high-energy architectural elements (cut and fill). A picture is provided in Figure 4D. Cut and fill depositional style indicates a braided and bed load dominated fluvial system that cannibalises its own deposits (multilateral and multistorey stacking pattern). Only the most downcut part (scour fill) is preserved in such a high-energy depositional setting. A multilateral stacking pattern typically occurs when a lack of accommodation space and a high amount of sediment supply prevails. Architectural elements such as floodplain fines (FF), lateral accretions (LA) and abandoned channels (AC) are rarely preserved as they are readily reworked in such a fluvial system.

The log section 48–83 m shows an increase in intermediate-energy architectural elements such as FF and LA. Additionally, between 64 m and 83 m several AC are preserved (example in Figure 4A). Because they are

found there, we see for the upper part (48–83 m) of depositional environment 1 an increase in preservation potential compared to the previous bed load fluvial system (0–46 m), interpreted as an increase in accommodation space.

Depositional environment 2 (Figure 5): The log section 83–100 m shows fluvial architectural elements CH, SB, and dominantly FF, crevasse splays (CS) and levees (LV), (see Figure 4B). FF, CS and LV are low-energy architectural elements, typically located in the top part of a fluvial cycle and therefore usually reworked by fluvial dynamics. As FF, CS and LV are seen across the section up to 96 m, accommodation space is interpreted to have been abundant because they indicate a high preservation potential. High preservation occurs where much accommodation space balances the sediment supply, such as in very distal parts removed from the source region of fluvial systems or in delta plains. Compared to depositional environment 1 accommodation space increased again and facies zones shifted towards the source region (retrogradational stacking pattern).

Depositional environment 3 (Figure 5): The dominance of CS and coastal mudflats (CM) in log section 100–125 m indicates a switch to a palustrine or very distal

Depositional environment / Log section	Main diagnostic features	Interpretation
5 Palustrine Shallow lacustrine (143-162m) 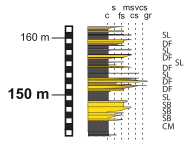 Palaeogeographical position 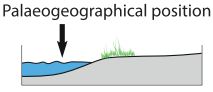	➢ Starts with the first clay bed (CM). The fines are interlayered by massive to ripple laminated sheet-like sand packages, showing internal coarsening upward trends. ➢ Towards the middle, an overall coarsening upward trend is established, then fining upwards to the top. ➢ Ripple laminated sands show bivalve traces (skolithos ichnofacies) as well as beetle and ant burrows. Numerous wavy ironhydroxide crusts between the clay and sand beds are present (thickness 1-3 cm).The sediments show minor gypsum precipitations compared to the former sections which were often pedogenised. ➢ Lithofacies: Sm, St, Sr, Fm and Fl; architectural elements: SL, DF, SB (from distributary channel) and CM. ➢ Th readings increase to highest concentrations (~50 ppm). U shows a trend of continuous increase. K shows a decreasing trend. The MS shows constant low readings with significant scattering. ➢ Kaolinite increases partly up to 73% and shows the highest proportions in the whole succession. Smectite is decreasing to 23%.	The increased amount of pedogenesis in this section shows significant depositional starvation which points to a lack of supply. Additionally, lacustrine sediments and thin delta foresets indicate a dominance of accommodation space over sediment supply. Hence, this is the unit representing the most distal part of the local sediment routing system. Facies zones have been shifted far towards landward positions.
4 Lower delta plain Rivermouth (125-143m) 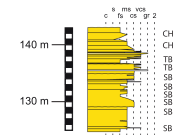 Palaeogeographical position 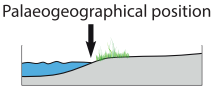	➢ Base erosional. The middle part is dominated by prograding, coarsening up successions of cross-bedded, well developed foresets of TB, with a maximal set thickness of 2m and common reactivation surfaces. The overall coarsening and thinning upward trend is followed by a less pronounced fining and thickening upward trend. ➢ Palaeocurrent measurements in TB point to westward flow directions with a dip of ~10-15° and a strike direction around 280°. ➢ Lithofacies: St, Sp, Sm, Fm, Gmg and Gpg; architectural elements: stacked SB, TB, CH and pedogenised CM. ➢ Two distinctive U anomalies were recognised (~127m) where U concentration increases to almost 75 ppm. From 139m the K concentration rises from ~2% up to ~6% in the pedogenised upper part. ➢ Smectite is the dominant clay mineral (83% and 73%) and kaolinite decrease to 16% to 20%. The illite content is increasing towards its highest value (~6%).	Multiphase, alluvial channels form the lower delta plain and prograde and retrograde into coastal lake settings (river mouth). The loosely spaced architectural elements indicate that sufficient accommodation space allow for a high preservation potential despite a higher amount of sediment supply. The initial palaeosol at the top implies times of missing or minimal sediment supply and point to depositional starvation or sediment bypass at other locations.
3 Lower delta plain Palustrine (100-125m) 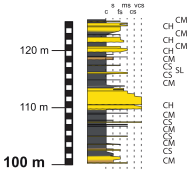 Palaeogeographical position 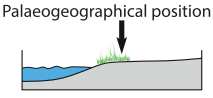	➢ The base is formed by an erosional bounded, structureless sand package (CS), top ends with a 15cm thick clay/silt bed (CM). In the upper half, sand body thickness increases towards the top. ➢ The middle part is built up by a 4m thick fining upward coarse sandstone deposit (CH) with internal trough cross stratification. Within certain sand bodies mud drapes and lenticular bedded flaser ripples occur. Two lenticular, coaly clay layers (Fm) appear locally at one side of the road cut (~124m). ➢ Lithofacies: Sm, St, Fm and Sr; architectural elements: CH, CM and CS. ➢ Ichnofossils (Skolithos) are present in sandy units. Gypsum precipitations in fines and sand are abundant. ➢ The lower clay prone part shows a pronounced peak in Th concentration. The MS is negative in the clay/silt sections and show higher readings in the sand dominated parts. ➢ Kaolinite proportion increases up to 36%, the smectite content decreases to 56%.	Mud drapes, flaser ripples and bivalve burrows point to lacustrine conditions. Deposition is characterised by the interaction of shallow lacustrine, fluvial and back swamp processes where clastic sedimentation sometimes ceased and organic-rich/coaly layers appeared. The thick fining upward channel deposit in the middle might be a distributary fluvial channel. This environment shows a high preservation potential pointing to plenty of accommodation space and a lack of sediment supply. Hence, deposition is controlled by availability of sediment supply.

FIGURE 5 The entire road cut section, split into units that form distinct depositional environments. Note that classification refers to the dominant depositional processes of a unit, a huge overlap and high frequency changes in depositional environments are part of a transitional alluvial-lacustrine system. Figure is structured in stratigraphic order progressing from the youngest (depositional environment 5) to the oldest unit (depositional environment 1). Their palaeogeographical position within the depositional system is illustrated; their main diagnostic features are described and interpreted also in terms of accommodation space. LF = lithofacies, AE = architectural element. Codes for LF and AE see Tables 1 and 2.

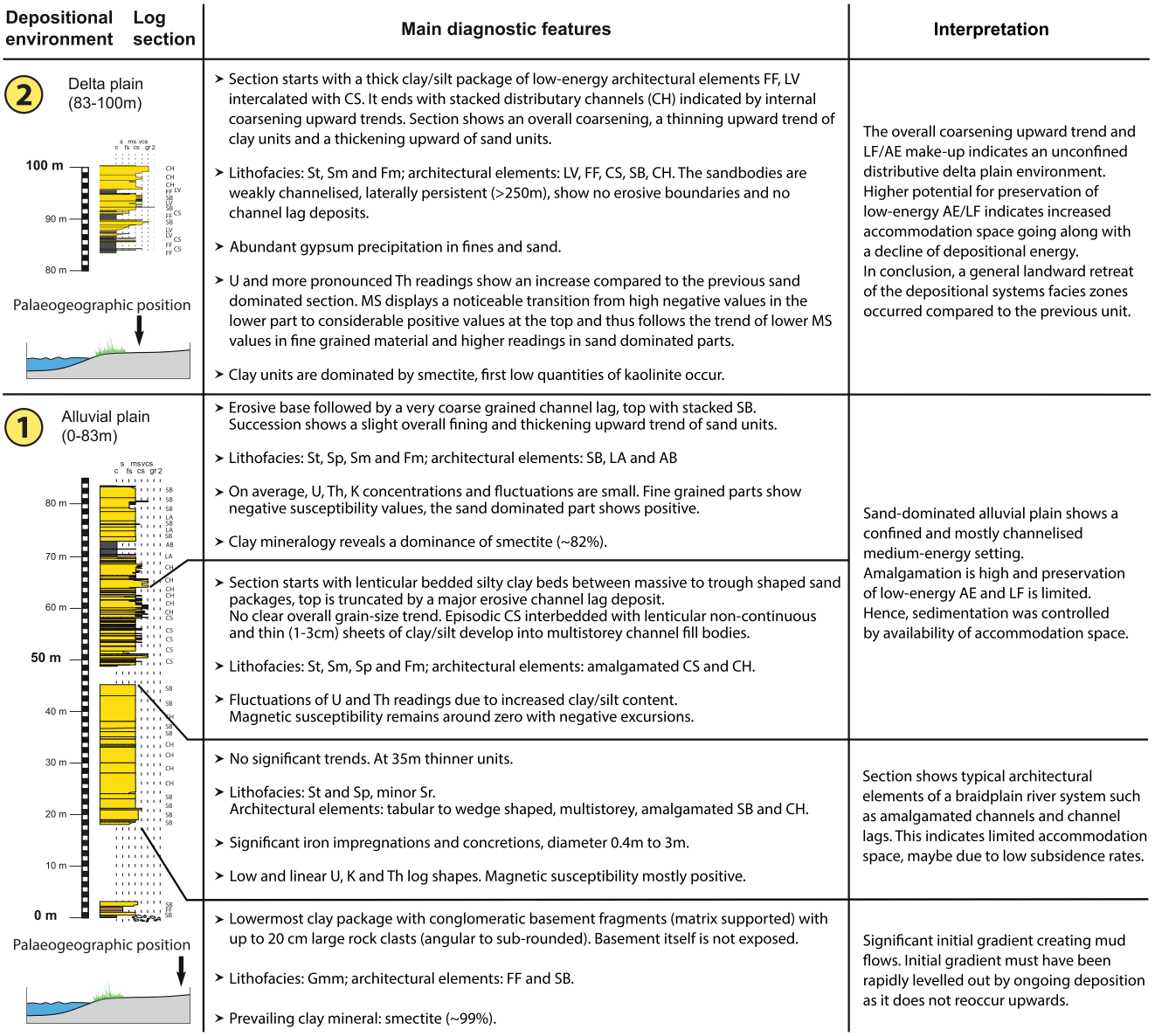

FIGURE 5 (Continued)

fluvial regime. The first occurrence of shallow lacustrine beds (SL) support this.

To preserve these architectural elements a high preservation potential is needed, which is only achievable under a high accommodation space. The available accommodation space can hardly be compensated for by sediment supply. Hence, the trend of increasing accommodation space and decreasing sediment supply continues.

Depositional environment 4 (Figure 5): The most striking feature in log section 125–143 m are the presence of thick and well-preserved, coarse sandy transverse bars (TBs). See Figure 4C. These TBs are interpreted as being part of accretional mouth bars and form where the stream power of a river collapses due to entering a standing water body such as a lake (Melstrom & Birgenheier, 2021). Hence, the TB is interpreted to be a part of the lower delta plain and can be formed only under conditions of a still high accommodation space, because the TB are thick and well-preserved. However, at the same time enough sediment supply had to be delivered to create them (pure sand-bearing).

Depositional environment 5 (Figure 5): The uppermost log section 143–162 m is dominated by what have been interpreted to be delta foresets (DFs), SL and CM architectural elements showing a palustrine realm. The DF, SL and CM architectural element association indicates that accommodation space cannot be compensated entirely by sediment supply. Hence, depositional environment 5 continues the overall trend of increasing accommodation space, decreasing sediment supply (= high A/S ratio) and subsequently the shift of facies zones towards the source region.

Figure 6 summarises quantitatively the development of depositional environments in terms of dominance

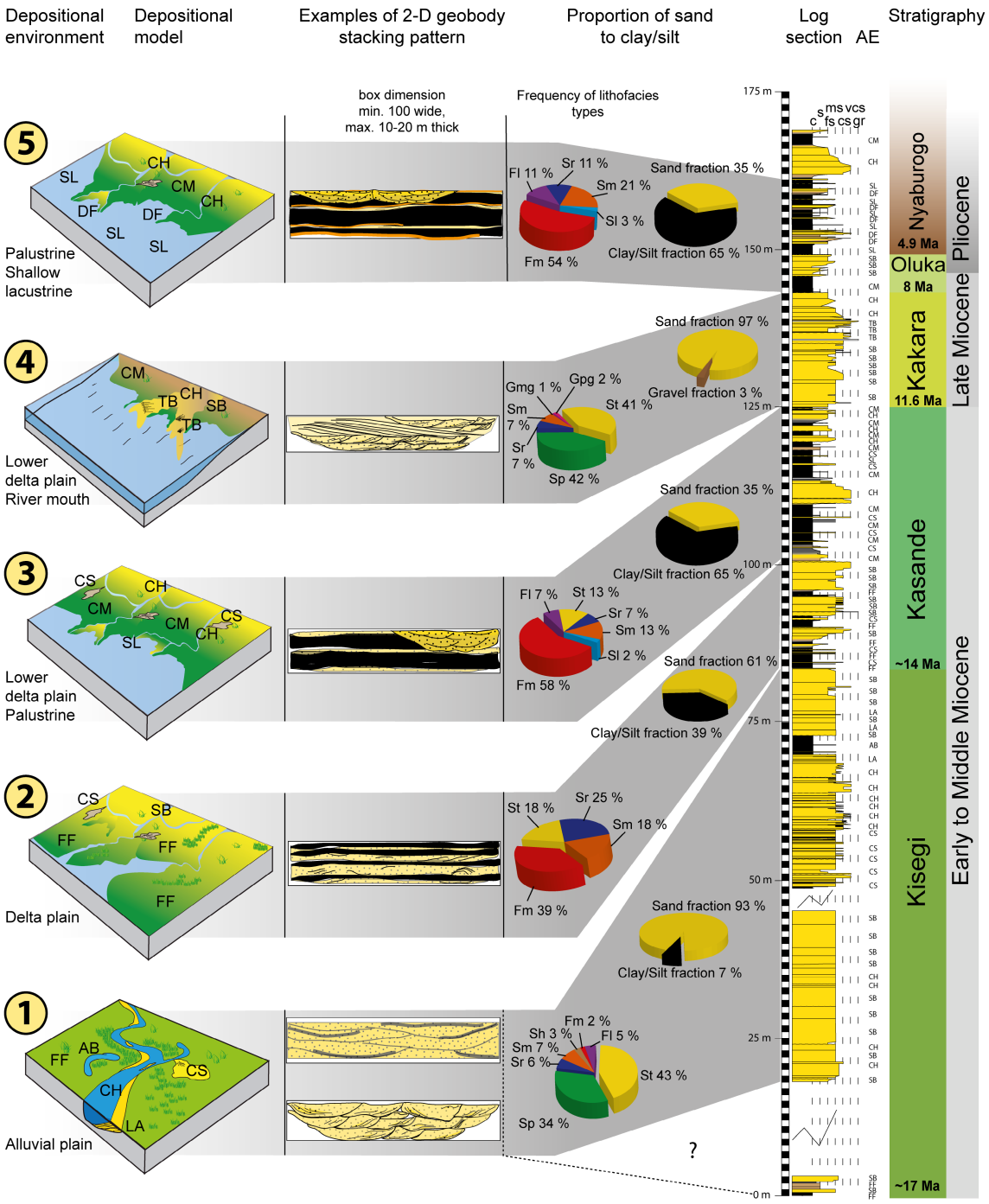

FIGURE 6 Depositional environments 1–5 from Figure 5 with sketched depositional model, their typical stacking patterns and frequency of lithofacies types (abbreviations explained in Tables 1 and 2) related to the compiled road cut section. At right the revised stratigraphic assignment to formations according to Lukaye et al. (2016). Ages are from Simon et al. (2017) and references therein.

and stacking patterns of architectural elements, proportions of lithofacies and ratio of sand vs silt/clay. Data are based on 2D analysis of outcrop wall-panels (Figure 2A–C, unpublished pictures, and complete section in Appendix S1).

Figure 6 reveals some large-scale depositional trends in the region. In more recent rocks, the sand fraction decreases and clay fraction increases, which indicates a reduction in the sediment supply. Lithofacies distribution displays a shift to low-energy types. Architectural elements become more loosely stacked indicating reduced reworking within the fluvial system pointing to an increase in accommodation space. Depositional environments show a retrogradational trend.

In conclusion, the changing lithofacies composition, proportion and stacking of architectural elements and evolution

of depositional environments indicates a long-term increase in accommodation space and decrease in sediment supply resulting in a retrogradational pattern of facies zones.

4.2 | Ichnofacies, pedogenesis and diagenetic features

Pedogenic, ichnofacies (skolithos, dung beetle burrows, nests), and early diagenetic features are mostly pronounced in the Oluka and Nyaburogo formations, and the Kakara Formation shows these features at an initial stage. Diagenetic features occur in fine sandy and silty beds and show up as colour-mottled structures caused by iron hydroxide precipitation and reduction of Fe^{3+} to Fe^{2+}, resulting in a spotty appearance with greenish light-reddish to light-violet and brown colours. Nodules are rare in silty and clayey lithofacies types and appear as dolocretes in well-sorted, fine sandy units aligned on foreset surfaces. In sandy layers close to clayey (lacustrine) beds, ferricretes occur frequently as nodules in the sand bed and as prominent surface crusts and are often associated with gypcretes. Ferricrete nodules are a typical feature of the Oluka and Nyaburogo formations and all lacustrine influenced/dominated beds in the Kisegi–Nyabusosi region. A gilgai microrelief (Paton, 1974) caused by swelling and shrinking processes under changing soil moisture can be observed in silty and clayey units, however, mature palaeosols are absent.

4.3 | Lithostratigraphy

The lithostratigraphy of the region has been constrained using the suggestions of Lukaye et al. (2016) and Simon et al. (2017) with the authors relying on the findings of the national stratigraphic commission of Uganda in outcrops and wells from oil exploration in the vicinity. Figure 6 correlates the row of depositional environments to this lithostratigraphy for the road cut. The trends and boundaries of depositional environments fit well to the suggested lithostratigraphic boundaries as traced by the National Stratigraphic Commission of Uganda (2011) and Lukaye et al. (2016) at the same outcrop. Note, that for the investigated outcrop the following stratigraphic correlation is established without biostratigraphic validation solely based on lithofacies descriptions and local average stratigraphic thicknesses given by Lukaye et al. (2016), Pickford et al. (1993), Roller et al. (2010) and by the National Stratigraphic Commission of Uganda (2011). Ages are from Simon et al. (2017).

Lukaye et al. (2016) suggest in their revised stratigraphy that the uppermost part of the outcrop already belongs to the Nyaburogo Formation. A clear indication for that boundary should be a silicified sandstone layer. However, this lithological feature could not be verified in this study as such beds also occur within the Oluka Formation. Another characteristic lithological fingerprint of the boundary does not exist. Hence, there is an uncertainty about the occurrence of the Nyaburogo Formation at the top of the road cut. On the other hand, some change in petrophysical data can be recognised at this boundary (Figure 7) as described from well logs in the area by Lukaye et al. (2016). If the topmost part of the succession is classified entirely as Oluka Formation its minimum thickness would be 26 m. However, if the topmost 20 m of the road cut is classified after Lukaye et al. (2016) as Nyaburogo Formation, the Oluka Formation shows a thickness of only 6 m. Basically, this model is possible, because significant erosion occurs between the Oluka and Kakara formations. In addition, non-deposition would provide another explanation.

Accepting the lithostratigraphic correlation, depositional units can be linked to formations as follows: Depositional environment 1 can be assigned to the Kisegi Formation (base at *ca* 17 Ma) with pure fluvial deposits and a minimum thickness of 88 m. Depositional environments 2 and 3 correspond to the Kasande Formation (base at *ca* 14 Ma) with a delta front, lower delta plain and some palustrine environment comprising 88–125 m of the section. Depositional environment 4 from around 125–143 m corresponds to the Kakara Formation (base at *ca* 11.6 Ma) with the first coastal mudflat, representing lower delta plain. The depositional environment 5 from *ca* 143 to *ca* 161 m to the Oluka Formation (base at *ca* 8 Ma) and Nyaburogo Formation (base at 4.9 Ma) with shallow to deep lacustrine beds containing iron crusts. Total thickness of the Oluka Formation in the Kisegi–Nyabusosi area is about 50–60 m (Lukaye et al., 2016; Pickford et al., 1993), hence only 6 m are represented in the outcrop. However, the exposed lower part shows a prominent erosional surface that can be linked to the biostratigraphic hiatus of mollusc zone G2a (*ca* 10–8.5 Ma) as discovered by Pickford et al. (1993) and Van Damme and Pickford (2003). The coincidence of a missing mollusc zone and presence of erosional features may represent a major unconformity, which can be traced as a chrono-stratigraphic horizon throughout the basin ('S3un' unconformity of Simon et al., 2017) indicating a regional base-level fall resulting in negative accommodation space.

4.4 | Bulk mineralogical analysis and clay mineralogy (XRD)

In total 33 samples were analysed. Eight rock powder samples show that detrital quartz, potassium feldspar and albite account for 50%–60% of whole rock; smectite,

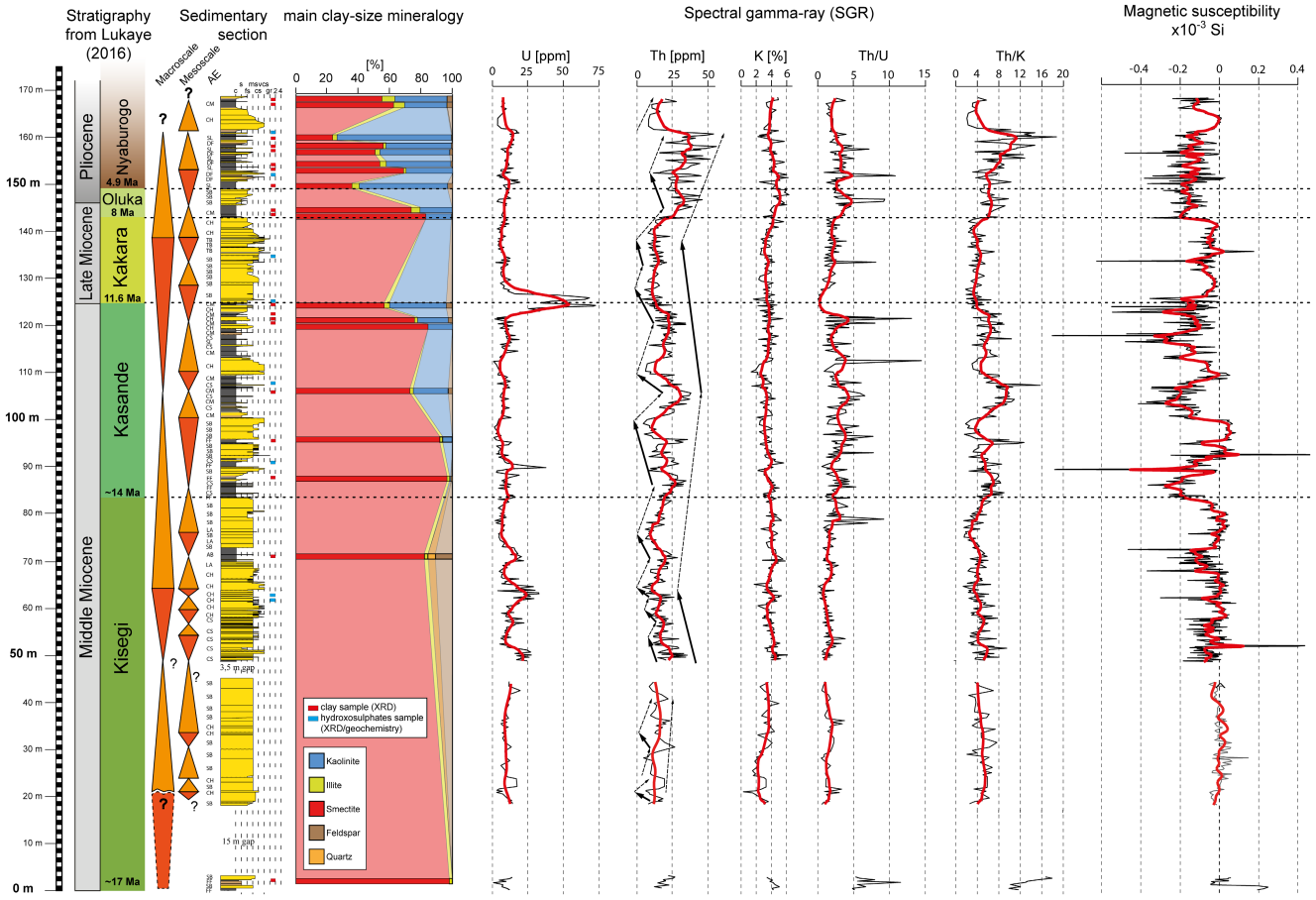

FIGURE 7 Stratigraphy, cycle analysis, architectural elements, sedimentary log, main clay-size mineralogy, spectral gamma-ray data and magnetic susceptibility of the road cut section. In the clay-size mineralogy box, results from bulk-rock and clay mineral XRD-analysis were compiled and jointly normalised. In some samples amounts of max. 1.2% of albite and/or goethite occur, which cannot be displayed in the diagram, but they were part of the normalisation. For bulk-rock and hydroxosulphate sample results, see main text. Superposed on the petrophysical log is a Gaussian filter for data smoothing (red graph). Note that trends in the Th-log follow extremely well stratigraphic base-level cyclicity. Solid arrows indicate fall-times, dotted ones rise-times. This mimics a strong sediment supply signal as here Th concentration is considered to reflect a pure detrital signal. In addition, the behaviour of magnetic susceptibility correlates well with the Th-log. For interpretation see text. Stratigraphic assignment to formations according to Lukaye et al. (2016) with ages from Simon et al. (2017).

kaolinite, illite and chlorite make up the remaining proportion. In the lowermost samples (*ca* 2 m and *ca* 71 m), minor concentrations of gypsum (*ca* 4%) and jarosite (*ca* 2%–6%) were detected.

Seven samples were taken from beds with a striking whitish appearance and a peculiar low density, showing grain sizes from silt to fine sand and irregularly interfingering with sandy, silty and clayey parts of the outcrop. In the field, this whitish, low-density matter is suspected to represent volcanic tuff. However, five out of seven samples (*ca* 62 m, *ca* 91 m, *ca* 108 m, 125 m and 135 m) turned out to be largely composed of hydroxosulphates with natronalunite the main component. Other components are jarosite, natronjarosite and phlogopite. The XRF measurements show an unusual geochemistry: SiO_2 1–20%, Al_2O_3 *ca* 30%, and S *ca* 14%. Loss of ignition (LOI) is high at *ca* 43%. The other two of the seven specimens (*ca* 152 m and *ca* 161 m) have much higher SiO_2 (*ca* 75%) and Al_2O_3 (*ca* 8%) values. The LOI makes up 7% while the sulphur content is only 0.08%.

Another 18 samples prepared for clay measurements show three dominant clay types that make up over 90% of each sample: smectite, kaolinite and illite (Figure 8). The most common clay mineral is smectite with a general proportion of 23% to over 97%, followed by kaolinite ranging from 0% to 73%, whereas illite occurs in lower amounts comprising 1% to 8%. Minor components (around detection limit) were lepidolite, anatase, greenalite, muscovite, phlogopite, and chlorite–vermiculite–montmorillonite-mixed layers. The XRD detection limit ranges from 0.5% to 4% depending on phase type, crystal size and crystallographic ordering. Clay composition shows a prominent trend from a smectite-dominated environment in the lower half (0–90 m) towards a kaolinite-dominated environment in the upper half (90–169 m), especially in the Oluka Formation

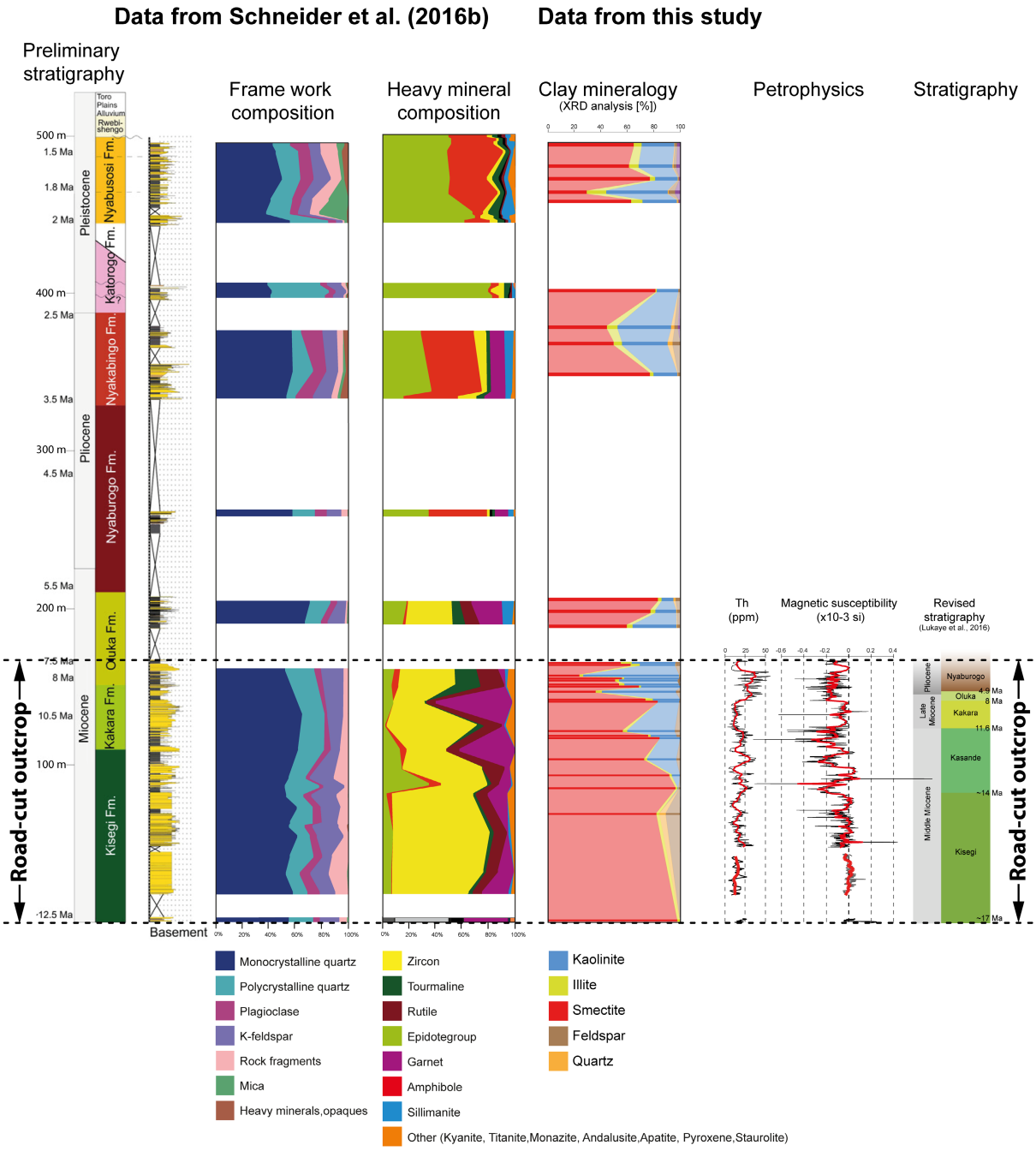

FIGURE 8 Compilation of heavy mineral data from Schneider et al. (2016a, 2016b) with their preliminary stratigraphic scheme (left), revised stratigraphy of Lukaye et al. (2016) with ages from Simon et al. (2017) at right, and data from this study along the road cut succession (middle). Note that major changes in heavy mineral composition occur much higher up in the stratigraphy than the road cut exposes. However, in the topmost part of the road cut, tourmaline comes in, where kaolinite is dominant and high thorium readings occur. Details see text.

(Figure 7). Feldspar (anorthoclase; up to 18%), is only present in the Kisegi Formation. Note that the increase in kaolinite occurs together with an increase in Th and a decrease in magnetic susceptibility. The clays are interpreted as allochthonous due to missing diagenetic and authigenic mineral associations, that is, illite–smectite-mixed layers or palygorskite. A high amount of detrital quartz and feldspar (50%–60%) in the bulk samples supports this.

4.5 | Cycle analysis

Based on the observations of trends in accommodation space and sediment supply, a fourfold hierarchy of overall, macroscale, mesoscale and microscale stratigraphic base-level cycles could be identified in the road cut succession. Cycles exceeding the exposed section are called ‘overall’. Cycles assembling this overall cycle were called

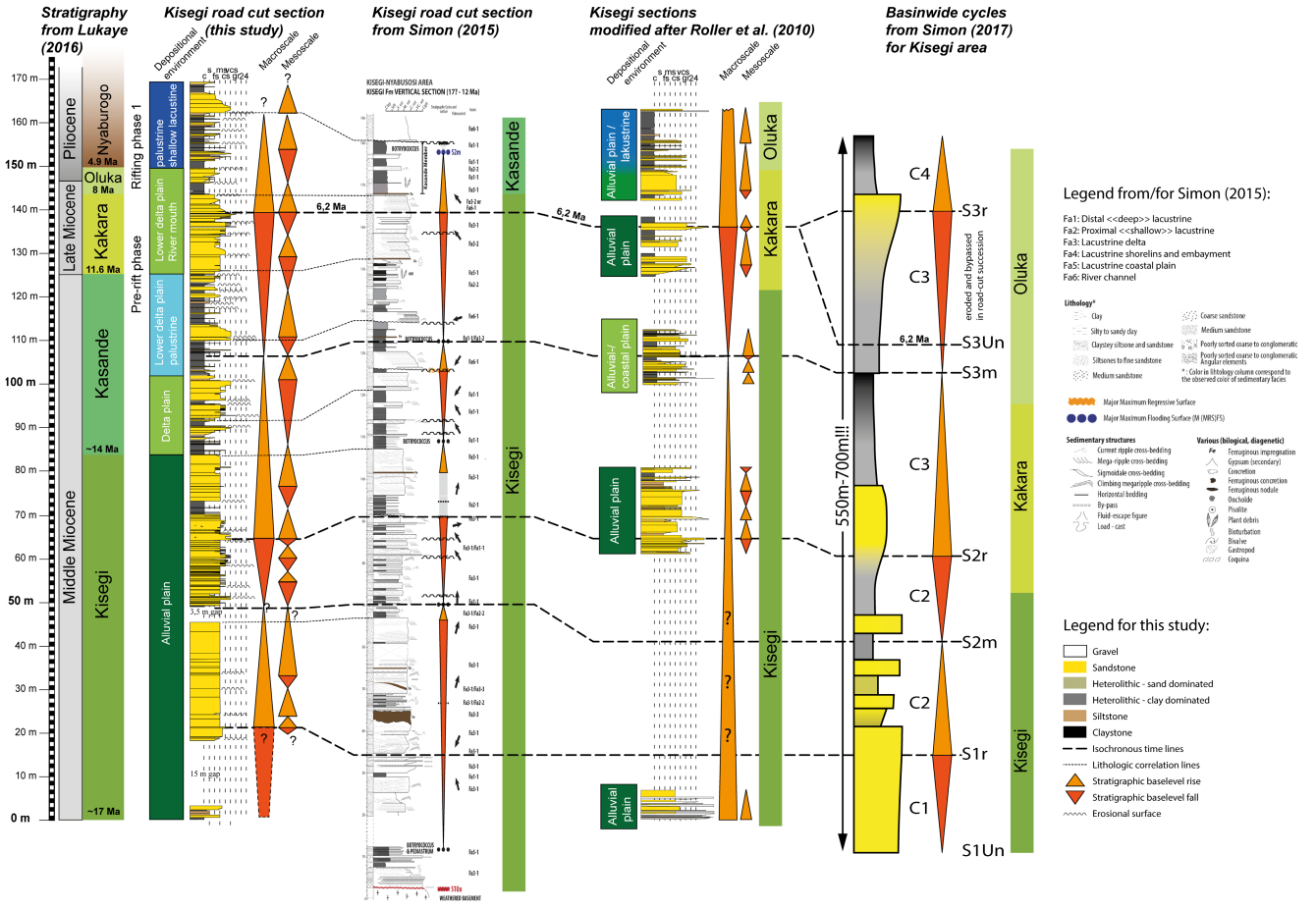

FIGURE 9 Sequence stratigraphic correlation of the road cut section to the study of Simon (2015) at the identical outcrop, to neighbouring sections of Roller et al. (2010), and to basin-wide traceable cycles found and mapped by Simon et al. (2017) using outcrops in the study area, wells and seismic sections of the Lake Albert Basin. Isochronous correlation (between turn-around points) are shown with thick large dotted lines, lithological correlation with thin, small dotted lines (between the two sections of the very same outcrop). Stratigraphy of this study follows Lukaye et al. (2016) as established in the same outcrop. Note significant discrepancies in thickness of basin to outcrop sections and the assignment of lithology to formations between the different studies. In the study area mollusc zone G2a is missing dated to *ca* 10 to 8.5 Ma pointing to a significant hiatus, which plot in the upper Kakara Formation. Ages are from Simon et al. (2017).

'macroscale', while the next smaller-scale cycles are called 'mesoscale'. 'Microscale' cycles are the smallest cycles that could be found in the sedimentary record. This nomenclature is independent of thickness and represents a superposition concept of hierarchical cycles. In this case, macroscale cycles are approximately 50 m thick, mesoscale cycles 5–20 m, and microscale comprise a few metres. Figure 7 (and Figures 3 and 9), display only macroscale and mesoscale cycles, because they are of major importance in the study area. Microscale cycles are not considered, because they normally represent self-organised depositional processes (autochthonous) and are therefore of very limited value for regional correlation due to their small lateral endurance. Overall cycles are not used because for correlation, turn-around points of cycles are needed. The overall scale cycle's turn-around points are not exposed and therefore it cannot contribute to regional correlation.

Three macroscale cycles are found. The lowermost shows a thickness of 50 m while the second and third macroscale hemicycles extend over 56 m, and >63 m respectively. Hence, along the entire section (overall scale), the macrocycle thickness increases. At the same time, frequency and thickness of low energy deposits increase as well. In the lower part of the succession, macroscale base-level cycles are asymmetric (Figures 3, 7 and 9), meaning the rise hemicycle is thicker than the fall hemicycle; meaning fall hemicycles were less well preserved. In the upper part of the succession, a tendency towards higher preservation potential of fall hemicycles is observed making cycles more symmetrical. The upward-increasing preservation potential indicates an overall stratigraphic

base-level rise hemicycle comprising the Kisegi to Oluka formations (entire outcrop).

Often five mesocycles make up one macrocycle (Figures 3, 7 and 9). Like macrocycles, mesoscale cycles appear also more symmetrical towards the top of the succession. In addition, mesoscale cycles tend to be thinner during macroscale base-level fall times (thick parts of triangles) due to a reduction in the accommodation space. Note that preservation potential of fall hemicycles (i.e. thickness) increases towards the top of the succession also at this scale.

4.6 | Petrophysical parameters

In Figure 7, spectral gamma ray data, total U, Th, K content, Th/U and Th/K ratio, respectively as well as magnetic susceptibility logs are shown together with the sediment log, clay mineral composition, cycle analysis and stratigraphy.

4.6.1 | Spectral gamma ray

Total U (^{234}U, ^{235}U and ^{238}U) shows a rather constant record of 10 ppm on average. There is a tendency towards *ca* 5 ppm higher values in the clay/silt dominated parts, hence, readings seem independent of depositional environment and facies. Remarkably, the U content increases significantly at two stratigraphic intervals. The lower anomaly (50–68 m) shows values up to 30 ppm, the upper anomaly (122–127 m) up to 75 ppm, and both comprise clay as well as sand beds. Therefore, U has not been considered for sequence stratigraphic interpretation, nor as a lithostratigraphic marker. However, the upper, larger anomaly coincides with the Kasande–Kakara boundary.

In contrast, Th displays pronounced and very systematic excursions in its signal. The clay/silt parts consistently show higher values when compared to the sand dominated intervals. Using the Gaussian filter, a clear trend is obvious from constant low values in the sand package (18–43 m) towards highest readings in the uppermost clay dominated facies (141–161 m). As Th is almost insoluble, it is usually enriched in soils as residue (Ruffell & Worden, 1999). However, in this case no significant increase in Th concentrations could be detected at palaeosol levels. Thus, Th readings are interpreted as a pure detrital signal, caused by stripping of soils in the hinterland.

In contrast to Th, K shows no clear dependency on grain size. Strong fluctuations or anomalies as they occur in the U or Th measurements are missing. Applying a Gaussian filter, a slight trend from around 2% in the lowermost sand package (18–43 m) towards higher values (max. up to 6%) in the uppermost clay/silt dominated section from 141 to 161 m can be observed and dedicated to the increase in clay minerals.

4.6.2 | Magnetic susceptibility

In general, magnetic susceptibility shows higher readings in sand dominated intervals and lower ones in clay/silt dominated intervals. Normally, quartz, feldspar and clay minerals show similar, very low negative (diamagnetic) readings. Hence, the sand must contain significant amounts of paramagnetic components shifting the readings even to slightly positive values in the lower half of the succession. Based on the sand fraction, an upward decrease of −0.1 si units is noticed (see e.g. 20–40 m compared to 120–140 m), which can be recognised also for the clay/silt fraction (compare e.g. 50–60 m to 150–160 m). Hence, declining magnetic susceptibility can be interpreted as a result of the overall fining upward trend. The carrier of the paramagnetic signal in the sands is unknown, but note that this (weak) trend is opposing the upward increase in Th. In general, trends in magnetic susceptibility mimic roughly trends of Th. In detail, low Th measurements correspond to high susceptibility readings and vice versa. Regarding the strong scattering of the susceptibility signal, bed thickness and fluctuation of lithofacies play an important role, thus, the noise of the susceptibility log can also be used to characterise depositional environments.

5 | DISCUSSION

5.1 | Base-level cycles and tectonic signals

In the lower half of the road cut succession (Kisegi Formation), both scales of fall hemicycles are less preserved (due to pervasive erosion) leading to asymmetrical cycles (Figure 7). In conclusion, in the lower stratigraphic interval (especially the lower Kisegi Formation), overall cycle stacking indicates sediment oversupply and limited accommodation space, which means the small amount of available accommodation space governs deposition as both are needed to create a rock record. In contrast, in the upper half (Kasande, Kakara, Oluka and Nyaburogo formations), fall hemicycles are thicker (=better preserved), hence, cycles become more symmetrical indicating a more balanced ratio of accommodation space to sediment supply, which results in aggradational stacking patterns. Considering the entire succession, the increasing preservation of fall hemicycles indicates an increase in

accommodation space which shows that an overall base-level rise cycle exists.

In the Kakara Formation, sandy intervals are slightly coarser than in the Kisegi Formation and erosional surfaces around the boundary between the two formations indicate increased stream power, which points to steeper gradients. However, the macroscale fall hemicycle is well preserved, that is, it is the thickest of the entire road cut succession, showing that sufficient accommodation space was available to preserve thick, coarse-grained, high-energy lithofacies types. Therefore, this major change to balanced proportions of A and S in the Upper Kakara and basal Oluka formations is interpreted to be caused by increased subsidence.

In the Oluka and Nyaburogo formations, the sedimentary system changes to one dominated by accommodation space, which means deposition is now governed by the availability of sediment supply coinciding with the onset of shallow lacustrine conditions. Compared to data from Pickford et al. (1993), Roller et al. (2010), Lukaye et al. (2016), and Simon et al. (2017) the increase in accommodation space continues stratigraphically upward. The large-scale change (Figure 9) towards dominance of accommodation space below the Oluka Formation must be governed by regional controls. Such controls are subsidence and lake-level change, which contribute to accommodation space whereas climate and tectonic uplift contribute to sediment supply (Figure 3B). In addition, Roller et al. (2010) suggested a macroscale cyclicity (Figure 9) in outcrops located 0.3 km west to 4.6 km south-east around the road cut. There, macroscale base-level cycles show a similar pattern in terms of cycle symmetry and evolution of depositional architecture. Hence, it is possible to correlate turn-around points of both locations at macroscale. The lateral traceability of turn-around points (Figure 9) makes it probably that external controls are responsible for the observed cyclicity.

The road cut succession shows distinct trends in the relationship between accommodation space and sediment supply, which results in sections where accommodation controls deposition and others with a supply control. The stage with accommodation space control (Kisegi Formation) is assigned to the pre-rift phase, where limited subsidence occurs. During the Kasande and Kakara formations acceleration of subsidence can be observed, but still on a pre-rift level. The Oluka and Nyaburogo formations in the upper part of the outcrop then mark the transition to the rift phase 1, where deposition is supply controlled, which is in accordance with the findings of Simon et al. (2017).

Based on reflection seismic surveys, outcrops and wells, Simon et al. (2017) define the shift from pre-rift to syn-rift (rift phase 1) at the basin-wide traceable unconformity 'S3Un' and correlate it with the lower Oluka Formation. Revised biostratigraphical evidence dates this event to around 6.2 Ma. However, according to Lukaye et al. (2016), the basin-wide traceable unconformity 'S3Un' must be correlated to the upper part of the Kakara Formation (Figure 9), where in the road cut a significant erosional surface with several metres downcutting exists (Figure 2B). In addition, the closely following base of the Oluka Formation is also erosive with most of it suspected to be missing (Lukaye et al., 2016; Pickford, 1993; Figure 2C), an observation supported by the absence of mollusc zone G2a (10–8.5 Ma). It is probably to make the basin-wide 'S3Un' unconformity (Figure 9) responsible for both erosional surfaces and/or non-deposition.

Arguments also come from geophysical and petrographic data: The section of the Oluka Formation above the unconformity 'S3un' shows enhanced Th readings (factor 2–4 to normal log response). The enhanced Th signal can be explained by incision of pediments and stripping of soils, which is believed to be roughly synchronous with the unconformity (Guillocheau et al., 2018; Taylor & Howard, 1998). Stripping of soils is an important surface process at the onset of rifting on the East African Plateau during the middle and upper Miocene (Simon, 2015; Taylor & Howard, 1998). Thorium has a distinct affinity with soil particles, particularly clayey soil, which causes Th to be less mobile and concentrate in soil more than 5000 times higher than in interstitial water (Peterson et al., 2007). After stripping, the very fine-grained clastic fraction of these soils typically settles in very-low energy environments. Applying this concept, low readings of Th represent times when most of the sediment bypasses and only coarse-grained (high-energy) lithofacies types can be preserved. In conclusion, a trend towards low Th readings means progradation of facies belts towards the basin centre, which represents a base-level fall. This also works in reverse: A trend towards high Th readings means an increase in fine-grained basinal facies and retrogradation of facies belts to landward positions during rise hemicycles. In Figures 3C and 7, the Th trends are marked with arrows along the log to enhance the signals shape. Continuous, thick lines represent fall-times (decrease in readings) and dotted lines rise-times (increase in readings). Note that the depicted Th trends mirror almost perfectly the interpretation of the sedimentary record in terms of base-level cycles, so that it is possible to use them for sequence stratigraphic interpretation in well logs without lithofacies identification.

Provenance data from the same outcrop published by Schneider et al. (2016a, 2016b) show no distinct change of heavy mineral spectra over the outcrop, except a significant increase in tourmaline in the Upper Kakara Formation (Figure 8). The major shift in heavy mineral spectra to a

dominance of amphibole and epidote is observed between the Oluka and Nyaburogo formations in surrounding sections (Figure 8). If correlation of the 'S3Un' unconformity to the uppermost part of the road cut is correct, this would mean that provenance pattern and hence the general drainage configuration persisted for some time across this basin-wide event, interpreted as the transition from pre-rift to syn-rift phase 1 by Simon et al. (2017). Hence, this study supports the hypothesis of Schneide et al. (2016b) that a lag time exists until river catchments adjust to the new tectonic rift-stage while changes in supply systems are more gradual, taking up to 1 Myr. A smooth transition from the pre-rift to the syn-rift phase is also supported by the trend towards increasing accommodation space that culminates in the topmost part of the outcrop (Nyaburogo Formation), which is already the beginning of the (syn-)rift phase 1.

5.2 | Sequence stratigraphy versus lithostratigraphy

Simon's (2015) cycles are progradational–retrogradational cycles and are therefore comparable to the stratigraphic base-level cycles applied in this study. Based on the revised lithostratigraphic and age model of Lukaye et al. (2016) for the road cut, the macroscale cycles of this study correspond to the basin-wide traceable cycles C1 to C3 of Simon et al. (2017). Figure 9 compiles the lithostratigraphic age models of both studies and suggests a correlation of the sequence stratigraphic cycles. The progradational hemicycle C1 of Simon et al. (2017) starts with the basement and ends up in the lower to middle Kisegi Formation (Figure 9). Subsequent complete cycles C2 and C3 and the retrogradational hemicycle C4 can be directly correlated with the stratigraphic base-level fall-rise macrocycles established in this study.

However, when applying this sequence stratigraphic correlation, a bias in lithostratigraphy and stratigraphic thickness becomes obvious. In Simon (2015), the entire road cut is assumed to be part of the Kisegi and Kasande formations, because the Kisegi Formation alone is considered to reach a thickness of almost 200 m according to field studies and correlations to wells (Simon et al., 2017). In this model, the entire road cut corresponds to their C1 progradational hemicycle and C2 retrogradational hemicycle, which is reasonable if their age model of the road cut is correct.

5.3 | Palaeoenvironmental proxies and climate signals

The climate of the investigated Miocene to lowermost Pliocene interval from *ca* 14.5 to 4.9 Ma encompasses an overall increase in humidity, reflected in multiple climate-sensitive parameters such as depositional environments, spectral gamma ray, bulk mineralogy and clay mineralogy (Figure 7). Depositional environments show a backstepping trend from fluvial to palustrine/lacustrine facies belts (Figure 6). Starting with a proximal braided river plain, the system grades into a distal river plain, and finally a delta plain with successive and overlapping crevasse splays. Evaporites or mature pedogenic horizons are missing which also indicate an overfilled basin with sufficient water available. Around the boundary of the Kisegi and Kakara formations around 12–11 Ma, this delta plain was flooded by a palaeo-lake (Lake Obweruka according to Pickford et al., 1993). Until *ca* 5 Ma, fluctuation between a lower delta plain and shallow lacustrine conditions continued. In the road cut succession, the highest water-level was reached in the Oluka Formation at around 7 Ma, yet still reflecting shallow water conditions. Due to multiple erosional surfaces, some showing downcutting up to several metres, short-term lake-level lowering must have occurred frequently. Short and small incisions should be due to seasonal lake-level fluctuations or decadal dry periods because over the long-term enough accommodation space is available to preserve even larger amounts of sediment supply.

Around 3 km to the east, Roller et al. (2010) found additional evidence for a humid climate during deposition of the Oluka Formation, indicated by frequent iron impregnation and beds with ferric pisolithic and ooidic components. Abundant iron crusts and pedogenised shale beds were also recorded in the upper part of the road cut succession (Nyaburogo and Oluka formations, representing depositional environment 5). Increased groundwater flow in the proximity of the supposed nearby Lake Obweruka probably enhanced lateral and vertical transport of dissolved iron close to groundwater barriers (e.g. groundwater–lakewater chemocline) and promoted the precipitation of ferricretes.

Spectral gamma ray logs of total U, Th and K concentrations can be used to evaluate formation boundaries, diagenesis, mineralogical composition, rock types or palaeoclimate changes (Schnyder et al., 2005). A higher groundwater table may lead to accumulation of U at the vadose–phreatic interphase; hence, increased U concentrations can be a marker for a palaeo-watertable (Doveton, 1994). The gamma-ray data of this study do not support such a trend of U concentrations. Amplified fluctuations in mixed sandy to clayey/silty sediment intervals might be caused by local U mobilisation (see intervals 50–68 m and 122–127 m). A prominent excursion in the Kakara Formation during base-level fall might be explained by increased exposure of the delta plain and impregnation at a shallow groundwater table. Alternatively,

U can also be introduced into sediments by detrital input of organic matter (Rider, 1996). At 124 m a thin, organic-rich clay layer occurs which might be the source of increased U at this stratigraphic level. In this case, the elevated U concentrations would not be significant palaeoclimatically because U could be diagenetically trapped by reduction and immobilisation within the organic-rich clay at any time after deposition. However, here it marks the boundary between the Kasande and Kakara formations.

Concentrations of Th increase up-section by a factor 4. Because Th is almost insoluble (<0.15 ppb) in all natural settings (Viers et al., 1997), it is mechanically enriched as a residue under intensified chemical weathering and soil formation due to leaching and loss of the more soluble constituents such as Si, K and U (Ruffell & Worden, 1999). Therefore, the Th increase in soils can be interpreted as an increase in chemical weathering and thus, humidity. Enrichment of Th may occur in-situ by leaching of other components and or by redeposition of stripped soils in the drainage area. Stripping of soils needs a humid palaeoclimate in the hinterland (Parkinson, 1996; Schnyder et al., 2005). However, experiments investigating Th^{4+} sorption onto various metal oxides, for example, magnetite, goethite, hematite, aluminium oxides (Hongxia et al., 2007; Hunter et al., 1988; Murphy et al., 1999; Rojo et al., 2009) showed that Th sorption is pH dependent and co-precipitates with these metal oxides. We can exclude this in-situ model, as metal oxides would produce high, eventually positive magnetic susceptibility readings along with the Th enrichments, which is not observed. Hence, in this case, Th is a pure detrital signal and not affected by in-situ mobility.

In contrast to U and Th, K shows only an insignificant trend and/or dependency on grain size and it is a mobile element. Thorium is insoluble, therefore the Th/K ratio (Figure 7) can be used as a proxy for chemical weathering intensity in the drainage basin, and hence, the overall rise of the ratio indicates a humidification trend. In contrast, the Th/U ratio shows some distinct spikes of strong Th dominance over U. Particularly, they occur in the middle part of the section, that is, when the depositional system represents a distal delta plain with temporary palustrine conditions, which favours U mobility. Consequently, the Th/U spikes can be interpreted as caused by U leaching, possibly due to oxygenation of pore waters after flood events. In such a scenario, Th/U spikes are a proxy for seasonality as far as a distal delta plain setting persists. The strongest spikes are observed in the Kasande, Oluka and Nyaburogo formations, where they coincide with frequent erosional surfaces, from which short-term lake-level fluctuations in these formations can be concluded.

Magnetic susceptibility integrates over bulk mineralogy, which makes it difficult to isolate contributions from different mineral types (Da Silva et al., 2013; Deconinck et al., 2003). The carrier of the paramagnetic signal in these sediments is unknown, but it shows the opposite trend to the upward increase in Th. Hence, along the succession, higher readings in magnetic susceptibility can be used (Figure 7) as a proxy for coarse-grained detrital input rather than as a proxy for local climate shifts explained by systematic variation of the mineralogical composition with grain size. The highest magnetic susceptibilities are expected from heavy minerals, which usually show paramagnetic behaviour. In the succession, thin in-situ iron impregnations (ferricretes) exist, often occurring as bundles producing the obvious spikes in magnetic susceptibility. However, such impregnations occur locally in the uppermost part of the section described here, pointing to dynamic interaction of groundwater with air or lake water. Hence, in this case, magnetic susceptibility can be used also as a proxy for fluctuating water level providing a climate signal.

The XRD mineralogy analysis clearly reflects an increase in chemical weathering, because along the section a change occurs from smectite-dominated clays (0–90 m) to kaolinite-dominated clays (90–169 m). Clay mineral distributions are widely used as palaeoclimate proxies (Chamley, 1989; Petschick et al., 1996) such as in-situ weathering or alteration of clays. In the road cut succession, the majority of clay minerals stem from soil erosion and are redeposited with some time delay after their formation because no mature in-situ palaeosols were developed. In addition, provenance data indicate admixed detritus from sources several hundred kilometres to the north-east (Gagnevin et al., 2017; Schneider et al., 2016a, 2016b). Hence, the climate signal deduced from the clay composition can be assumed to be of regional significance. Within the lower 100 m, a smectite-rich fine fraction dominates (up to 97%). Smectites are most probably derived from deeply weathered land surfaces where the relief was low, drainage poor and saline waters were present (Simon, 2015). Kaolinite increases in the Kakara, Oluka and Nyaburogo formations from 0% to 75% at the expense of mainly smectite and feldspar, which mirrors a humidification from the Middle to the Late Miocene (Early Pliocene) affecting large parts of the East African Plateau (Bonnefille, 2010).

The observation of intensified chemical weathering from clay mineral spectra agrees with the model of Taylor and Howard (1998) on weathered land surfaces in Uganda. Their study is based on a compilation of geotectonic, climate, sedimentological and chronological data. Within the time interval of the Kisegi and Kakara formations, they postulate stripping of former deeply weathered land surfaces of the Early Miocene, whereas

during the Oluka Formation, deep weathering of stable land surfaces is supposed. Moreover, chemical weathering was probably further amplified by increased tectonic activity in the Late Miocene (Simon et al., 2017) due to enhanced runoff, and rising topography, which resulted in kaolinite formation through intensified leaching and removal of K, Mg and Na. In the late Miocene, an increased gradient is supported by the larger grain size in the Kakara Formation.

A rare white, powder-like, and low-density sediment almost purely composed of hydroxosulphates was found at five levels. Occurrence is not specific to one distinct depositional environment and it appears from alluvial plain to distal floodplain/palustrine environments. Found hydroxosulphates are alunite [$KAl_3(SO_4)_2(OH)_6$] and natronalunite [$NaAl_3(SO_4)_2(OH)_6$], the two most frequent mineral types of the alunite group, beside jarosite [$KFe_3(SO_4)_2(OH)_6$]. Organic rich sediments can form sulphide-rich, acidic environments (H_2S). When destroyed by oxygenation, sulphuric acid is released and can directly react with illite to form alunite under a pH of 3–4. Jarosite is formed when pH drops further (Dill, 2001). In cases where acid groundwater carries high concentrations of K, Al, Fe^{3+} and SO_4, hydroxosulphates are formed under a saline environment (Long et al., 1992). In addition, direct precipitation under evaporitic conditions in Mg^{2+} and Ca^{2+} depleted brines can occur (Blanco et al., 2008). The depositional environment postulated here provides all these conditions. A hot, semi-arid climate on a distal river and delta plain can locally produce saline ponds during a temporal high-water table and in abandoned channels. Rotten vegetation favours sulphide-rich sediments, which can be oxidised in the dry season (Vasconcelos et al., 1993). In conclusion, these hydroxosulphate layers indicate a semiarid, seasonal climate with fluctuating humidity. The frequency of hydroxosulphate layers does not decrease up-section (Figure 7), which one would expect considering the observed overall trend towards more humid conditions. Most probably, their formation is tied to local conditions of water ponds and not to specific conditions at the terrestrial–lacustrine transition. Intercalation of hydroxosulphate, ferricretes and pedogenised horizons also in the upper section point to ongoing seasonality and dry intervals.

Based on key fossil flora and fauna, Pickford et al. (1993) suggest that rifting and rift topography was low and had little effect on climate in East Africa before the middle Pliocene and that a humid tropical climate existed which was linked to the Congo Basin. However, Miocene palaeoclimate records in East Africa are discontinuous and restricted to a few sites in Ethiopia, the Kenya Rift and the Semliki area of the Albertine Rift. Bonnefille (2010) reviewed palaeobotanical data collected at terrestrial sites and marine pollen records from the Atlantic and Indian Ocean and constructed a stacked curve of tree cover density in tropical Africa over the last 10 Myr, which can be used as a proxy record of humidity. Maximum tree cover of *ca* 20% is reached from 7 to 7.5 Ma and from 5 to 3 Ma. The rise in tree cover from 10 to 7 Ma found by Bonnefille (2010) is roughly contemporaneous to the trend seen here to wetter conditions. The Late Miocene peak in tree cover corresponds well to the presumably wettest period during the Oluka Formation dated from 8 to 4.9 Ma. However, so far this peak is not well constrained for East Africa and is most pronounced in West Africa.

Time-equivalent (*ca* 13–9 Ma) to the lower and middle part of the studied outcrop is the fluvial-lacustrine Ngorara Formation in central Kenya linked to the eastern rift branch. Rasmussen et al. (2017) logged nine sections and determined sediment facies, articulated fish fossils, palynology and clay mineralogy. They found an overall sub-humid climate becoming drier in the upper part. Over the entire time lakes persisted which fluctuated between freshwater and alkaline chemistry, the latter pointing to temporally increased evaporation and drier than average conditions. Pollen spectra are indicative of wooded grassland or grassy woodland, similar to the wetter intervals of the climate today in East Africa. Kaolinite is relatively rare and analcime and montmorillonitic smectite from weathering of volcanic ash dominate. The fragmentary record of Miocene palaeoclimate in East Africa, spatial heterogeneity and chronological uncertainties, prevent a conclusive linkage of the palaeoclimate trend reported in this study with others in the EARS and must be treated as a future corner stone of palaeoclimate research in East Africa.

5.4 | Implications for the initial stage in the EARS

This study provides a multi-proxy dataset for interpretation of climate and depositional environments as well as a sequence stratigraphic correlation of depositional cycles to basin cycles (Simon et al., 2017) for the Albertine Rift based on the newest available age model (Simon et al., 2017) and lithostratigraphy (Lukaye et al., 2016). The succession represents the pre-rift phase and the beginning of the (syn-)rift phase 1 of the Albertine rift according to correlation to a major basin-wide unconformity dated to 6.2 Ma. The cyclostratigraphic and palaeoenvironmental data of this study do not show a sharp and major break, however, a transitional trend during initial rifting is well recognisable:

- Accommodation space increases slowly along the entire pre-rift succession, but does not accelerate abruptly at the transition from the pre-rift to (syn-)rift stage 1 (Figures 7 and 9).
- In terms of base-level cyclicity, the change from pre-rift into the syn-rift stage can be defined by the shift from accommodation-controlled to supply-controlled conditions, which takes place before the 6.2 Ma unconformity and shows a transitional pattern (Figures 6, 7 and 9).
- Sediment flux and sediment composition show a long-lasting gradual trend and much delayed response with respect to activation of erosion and reorganisation of drainage systems (Figures 6–8). Increase in chemical weathering (Figure 7) and thus humidity goes along with more pronounced evaporative intervals in the depositional area. This can be interpreted as accentuation of the relief with uprising rift shoulders receiving additional rain and a subsiding rift basin suffering from aridisation in the rain shadow.
- Provenance data from Schneider et al. (2016a, 2016b) indicate a strong shift from ultrastable heavy mineral associations to amphibole–epidote-dominated spectra (Figure 8), which follows the expected pattern of fragmentation of large river systems due to rifting and activation of local sediment sources. However, based on the sequence stratigraphic model reported here (Figure 9), this reorganisation happened *ca* 1 Myr after the beginning of (syn-)rift stage 1.
- The pre-rift phase is dominated by fluvial deposits. At the onset of the (syn-)rift stage 1, distal alluvial systems and shallow lakes are favoured. Perennial lacustrine conditions occur in the (syn-)rift stage 1 (Figure 6).

This case study demonstrates that although distinct tectonic pulses of rifting can be identified, sedimentary source-sink systems are more persistent and gradual and/or delayed changes dominate over abrupt changes. In particular, large-scale drainage systems need time to be fragmented by accelerated faulting in the syn-rift stage. An overall trend in climate and depositional environments was identified, which can be linked to ongoing rifting. The long-term trend includes accentuation of the climate (e.g. seasonality) as well as an overall retrogradational trend from fluvial to perennial lacustrine conditions.

All these findings are in accordance with the active rifting model, which claims a long-lasting lithospheric thinning, which results in a slow transition from regional downwarping over diffuse rifting to discrete rifting (Ebinger et al., 2002). In the case of the Albertine Rift the pre-rift phase lasted over more than 10 Myr (from 17 to 6.2 Ma), before distinct faulting created the narrow rift as it exists today. The gradual response and long times involved cannot be explained by a distinct change in the far-field strain as required in the passive rifting model. On the other hand, the second major unconformity at 2.7 Ma and rifting phase 2 appear to be linked to the far-distance stress field of the South-west Indian Ridge (Stamps et al., 2008). At this time, extreme uplift of the Rwenzori Block started and provenance of sediments changed quickly (Bauer et al., 2010; Schneider et al., 2016b).

6 | CONCLUSION

Fluvio-lacustrine sedimentary environments of the basal succession in the Albertine Rift have been documented in detail and analysed with respect to physical parameters, bulk mineralogy and clay mineralogy. The succession shows a multilateral and multistorey sediment architecture at the base which develops into a dominantly aggradational pattern towards the top. Based on lithostratigraphic correlation and cycle analysis, the succession could be correlated with the Kisegi, the Kakara, the Oluka and Nyaburogo formations, which span from Middle Miocene (*ca* 17 Ma) to the Early Pliocene (*ca* 4.9 Ma). Major findings are as follows:

- Depositional environments involve alluvial plain settings in the Kisegi Formation, delta plain/palustrine in the Kasande, lower delta/river mouth settings in the Kakara Formation, and palustrine/shallow lacustrine settings in the Oluka and Nyaburogo formations. This back-stepping trend is regionally controlled by stratigraphic base-level changes, which indicate an increase in accommodation space in the rift basin towards the uppermost Miocene and early Pliocene.
- The Middle to Upper Miocene sediment succession confirms a pre-rift setting in the context of active rifting with slow, but increasing subsidence. Presumably, increasing accommodation space together with coarser grain size and stripping of deeply weathered soils as well as a shift to more local sediment sources signal initiation of the syn-rift phase, which started at 6.2 Ma according to a major basinal unconformity ('S3Un'). The unconformity marks an abrupt tectonic pulse in principal rift development.
- Bulk and clay mineralogy show feldspar–quartzose sands and smectite-dominated clays in the Kisegi Formation and feldspar-free sands and increasingly kaolinite-dominated clays in the Kakara and Oluka formations. Increasing proportions of kaolinite indicates higher chemical weathering and humidification of the climate towards the Upper Miocene.

- In the hinterland transport energy increased over time, as indicated by increasing grain size and by higher readings of Th in the spectral gamma ray, interpreted as a response to humidification together with stripping of soils due to increasing rifting activity. However, no sharp boundary between the pre-rift and syn-rift stage can be recognised.
- Geophysical parameters can be reliably used as palaeoenvironmental indicators. The retrogradational sediment architecture is reflected in an increase of Th readings in the spectral gamma ray. Mesoscale cycles, hydroxosulphate layers and spikes in the Th/U and magnetic susceptibility show superimposed short-term seasonal and/or climate cyclicity.
- Integrated evaluation of palaeoclimate proxies concordantly show humidification during the Middle and Upper Miocene with a peak at 4.9–8 Ma. Because of the scarcity of other records and uncertain chronologies, it cannot be verified so far, if the humidification trend is in accordance with other parts of the EARS or specific to the Albertine Rift.

By using a multi-proxy approach on this unique, rare and exceptionally large outcrop, light was shed on the depositional and climate history of the beginning of rifting in East-Africa. In particular, the studied succession can be taken as a reference for the slow and gradual response of depositional systems and palaeoclimate under active rifting in other settings.

ACKNOWLEDGEMENTS

This study is an outcome of the RIFTLINK research group, project B3 'Linking Source and Sink in the Rwenzori Mountains and adjacent rift basins, Uganda' and was funded by DFG grant HI643/7-2. We thank the Uganda National Council for Science and Technology (UNCST) and the Uganda Wildlife Authority (UWA) for research permissions and their support, as well as our Ugandan research partners from Makerere University for close and good collaboration. Furthermore, we must give thanks to the staff of the Petroleum Exploration and Production Department (PEPD) and the stratigraphic commission of Uganda, especially Joshua Lukaye. Tullow Oil Ltd., London, also has supported us. We thank Andreas Schumann and Kitam Ali for his superior support and assistance concerning all issues we faced in Uganda. The quality of a former version of the paper was significantly enhanced by an anonymous reviewer and by Eduardo Garzanti. The current version was edited and commented by Catherine Russell and Dave Somerville. We thank both reviewers explicitly as the quality of the manuscript benefited extremely from their thorough work on it. Open Access funding enabled and organized by Projekt DEAL. WOA Institution: TECHNISCHE UNIVERSITAET DARMSTADT Consortia Name : Projekt DEAL

DATA AVAILABILITY STATEMENT

Data sharing is not applicable to this article as no new data were created or analysed in this study.

ORCID

Jens Hornung https://orcid.org/0000-0003-3553-4654

REFERENCES

Allen, J.R.L. (1982). Sedimentary structures : their character and physical basis. *Developments in Sedimentology 30*, Vol. 1. Amsterdam: Elsevier, 592 pp.

Allen, J.R.L. (1984) Sedimentary Structures, their Character and Physical Basis. In: *Developments in Sedimentology 30*, Vol. 2. Amsterdam: Elsevier, 663 pp.

Bauer, F.U., Koehn, D. & Glasmacher, U.A. (2010) Long-term rift evolution. *International Journal of Earth Sciences*, *99*, 1483–1485. https://doi.org/10.1007/s00531-010-0601-7

Biscaye, P.E. (1965) Mineralogy and sedimentation of recent deep-sea clay in the Atlantic Ocean and adjacent seas and oceans. *Geological Society of America Bulletin*, *76*, 803–832.

Blanco, J.A., Armenteros, I. & Huerta, P. (2008) Silcrete and alunite genesis in alluvial palaeosols (late cretaceous to early Palaeocene, Duero basin, Spain). *Sedimentary Geology*, *211*, 1–11.

Bonnefille, R. (2010) Cenozoic vegetation, climate changes and hominid evolution in tropical Africa. *Global and Planetary Change*, *72*, 390–411.

Catuneanu, O., Abreu, V., Bhattacharya, J.P., Blum, M.D., Dalrymple, R.W., Eriksson, P.G., Fielding, C.R., Fisher, W.L., Galloway, W.E., Gibling, M.R., Giles, K.A., Holbrook, J.M., Jordan, R., Kendall, C.G.S.C., Macurda, B., Martinsen, O.J., Miall, A.D., Neal, J.E., Nummedal, D., Pomar, L., Posamentier, H.W., Pratt, B.R., Sarg, J.F., Shanley, K.W., Steel, R.J., Strasser, A., Tucker, M.E. & Winker, C. (2009) Towards the standardization of sequence stratigraphy. *Earth-Science Reviews*, *92*(1–2), 1–33. https://doi.org/10.1016/j.earscirev.2008.10.003

Chamley, H. (1989) *Clay sedimentology*. Berlin, Heidelberg, New York: Springer-Verlag, p. 623.

Chorowicz, J. (2005) The east African rift system. *Journal of African Earth Sciences*, *43*, 379–410.

Cloetingh, S., & Ziegler, P. A. (2009). 11 tectonic models for the evolution of sedimentary basins. Treatise on Geophysics, Volume 6: Crust and Lithosphere Dynamics, *6*, 485.

Cross, T.A., Baker, M.R., Chapin, M.A., Clark, M.S., Gardner, M.H., Hanson, M.S., Lessenger, M.A., Little, L.D., McDonough, K.J., Sonnenfeld, M.D., Valasek, D.W., Williams, M.R., and Witter, D.N. (1993) Applications of high-resolution sequence stratigraphy to reservoir analysis. In: Eschard, R. & Doligez, B. (Eds.), *Subsurface reservoir characterization from outcrop observations*. Proceedings of the 7th exploration and production research conference. Paris: Technip, pp. 11–33.

Cross, T.A. & Lessenger, M.A. (1998) Sediment volume partitioning: rationale for stratigraphic model evaluation and high-resolution stratigraphic correlation. In: Sandvik, K.O.,

Gradstein, F. & Milton, N. (Eds.) *Predictive high resolution sequence stratigraphy*. London: Norwegian Petroleum Society Special Publication, pp. 171–196.

Da Silva, A.C., De Vleeschouwer, D., Boulvain, F., Claeys, P., Fagel, N., Humblet, M., Mabille, C., Michel, J., Sardar Abadi, M., Pas, D. & Dekkers, M.J. (2013) Magnetic susceptibility as a high-resolution correlation tool and as a climatic proxy in Palaeozoic rocks – merits and pitfalls: examples from the Devonian in Belgium. *Marine and Petroleum Geology*, *46*, 173–189.

Deconinck, J.F., Hesselbo, S.P., Debuisser, N., Averbuch, O., Baudin, F. & Bessa, J. (2003) Environmental controls on clay mineralogy of an early Jurassic mudrock (blue Lias formation, southern England). *International Journal of Earth Sciences*, *92*, 255–266.

Dill, H.G. (2001) The geology of aluminium phosphates and sulphates of the alunite group minerals: a review. *Earth-Science Reviews*, *53*, 35–93.

Doveton, J. H. (1994) Geological Log Interpretation. SEPM short course, No. 29, 184 pp.

Ebinger, C., Petit, C., & Burov, E. (2002) Causes and consequences of lithospheric extension: the ups and downs of continental rifts. In: *Sedimentation in continental rifts*. Tulsa, OK: SEPM Special Publication. No. 73, pp. 11–23.

Ebinger, C.J. (1989) Tectonic development of the western branch of the east African rift system. *Geological Society of America Bulletin*, *101*, 885–903.

Feibel, C.S. (2011) A geological history of the Turkana Basin. *Evolutionary. Anthropology*, *20*, 206–216.

Gagnevin, D., Tyrrell, S., Morton, A.C., Leather, J., Lee, N., Floch, B.L., Frei, D. & Lukaye, J. (2017) Sand supply to the Lake Albert Basin (Uganda) during the Miocene-Pliocene: a multiproxy provenance approach. *Geochemistry, Geophysics, Geosystems*, *18*, 2133–2148.

Guillocheau, F., Simon, B., Baby, G., Bessin, P., Robin, C. & Dauteuil, O. (2018) Planation surfaces as a record of mantle dynamics: the case example of Africa. *Gondwana Research*, *53*, 82–98. https://doi.org/10.1016/j.gr.2017.05.015

Hein, F.J. & Walker, R.G. (1977) Bar evolution and development of stratification in the gravelly, braided, Kicking Horse River, British Columbia. *Canadian Journal of Earth Sciences*, *14*(4), 562–570. https://doi.org/10.1139/e77-058

de Heinzelin, J. (1959) Les formations du Western Rift et de la cuvette Congolaise. Actes IVe Congres Panafricain Prehistoire, Sect I. Ann. Du. Musee R. L'afrique Cent. Sci. Hum., *40*, 219.

Hinderer M. & Einsele G. (2002) Rifts as denudation-accumulation systems: concept, models and examples. In: *Sedimentation in continental rifts*. Tulsa, OK: SEPM Special Publication, no. 73, pp. 83–96.

Hongxia, Z., Jieqiong, Y. & Zuyi, T. (2007) Effects of phosphate and Cr^{3+} on the sorption and transport of Th(IV) on a silica column. *Journal of Radioanalytical and Nuclear Chemistry*, *273*(2), 465–471.

Hornung, J., &Hinderer, M. (2011) Depositional dynamics and preservation potential in a progradational lacustrine Fluvio-deltaic setting: implications for high-resolution sequence stratigraphy (upper Triassic, northwestern China). In: Davidson, S. K., Leleu, S., and North, C. P. (Eds.) *From river to rock record: the preservation of fluvial sediments and their subsequent interpretation*. Tulsa: SEPM Special Publication 97, pp. 281–310.

Hornung, J., Linsel, A., Schröder, D., Gumbert, J., Ölmez, J.A., Scheid, M. & Pöppelreiter, M.C. (2020) Understanding small-scale petrophysical heterogeneities in sedimentary rocks – the key to unraveling pore geometry variations and to predict lithofacies-dependent reservoir properties. In: Grötsch, J. & Pöppelreiter, M.C. (Eds.) *Digital geology – multi-scale analysis of depositional systems and their subsurface modelling workflows*. Houten: EAGE Book.

Hornung, J. & Aigner, T. (1999) Reservoir and aquifer characterization of fluvial architectural elements: Stubensandstein, Upper Triassic, southwest Germany. *Sedimentary Geology*, *129*(3–4), 215–280. https://doi.org/10.1016/s0037-0738(99)00103-7

Hunter, K.A., Hawke, D.J. & Kwee, C.L. (1988) Equilibrium adsorption of thorium by metal oxides in marine electrolytes. *Geochimica et Cosmochimica Acta*, *52*(3), 627–636.

Long, D.T., Fegan, N.E., McKee, J.D., Lyons, W.B., Hines, M.E. & Macumber, P.G. (1992) Formation of alunite, jarosite and hydrous iron oxides in a hypersaline system: Lake Tyrrell, Victoria, Australia. *Chemical Geology*, *96*, 183–202.

Lukaye, J., Worsley, D., Kiconco, L., Nabbanja, P., Abeinomugisha, D., Amusugut, C. & Sempala, V. (2016) Developing a coherent stratigraphic scheme of the Albert graben-east, Africa. *Journal of Earth Science and Engineering*, *6*(5), 264–294. https://doi.org/10.17265/2159-581x/2016.05.004

Macgregor, D. (2015) History of the development of the east African rift system: a series of interpreted maps through time. *Journal of African Earth Sciences*, *101*, 232–252. https://doi.org/10.1016/j.jafrearsci.2014.09.016

Melstrom, E.M. & Birgenheier, L.P. (2021) Stratigraphic architecture of climate influenced hyperpycnal mouth bars. *Sedimentology*, *68*, 1580–1605. https://doi.org/10.1111/sed.12854

Merle, O. (2011) A simple continental rift classification. *Tectonophysics*, *513*(1–4), 88–95.

Miall, A.D. (1977) Lithofacies types and vertical profile models in braided river deposits: a summary. In: Miall, A.D. (Ed.) *Fluvial Sedimentology*. Calgary: Geological Survey of Canada, pp. 597–604.

Miall, A.D. (1985) Architectural-element analysis: A new method of facies analysis applied to fluvial deposits. *Earth-Science Reviews*, *22*(4), 261–308. https://doi.org/10.1016/0012-8252(85)90001-7

Miall, A.D. (1996) *The geology of fluvial deposits: sedimentary facies, basin analysis, and petroleum geology*. New York: Springer, p. 316.

Miall, A.D. (2016) *Stratigraphy: a modern synthesis*. Cham: Springer, p. 454.

Moore, D.M. & Reynolds, R.C. (1997) *X-ray diffraction and the identifications and analysis of clay minerals*, 2nd edition. New York: Oxford University Press, pp. 204–224.

Mtelela, C., Roberts, E.M., Hilbert-Wolf, H.L., Downie, R., Hendrix, M.S., O'Connor, P.M. & Stevens, N.J. (2017) Sedimentology and paleoenvironments of a new fossiliferous late Miocene-Pliocene sedimentary succession in the Rukwa Rift Basin, Tanzania. *Journal of African Earth Sciences*, *129*, 260–281. https://doi.org/10.1016/j.jafrearsci.2017.01.010

Murphy, R.J., Lenhart, J.J. & Honeyman, B.D. (1999) The sorption of thorium (IV) and uranium (VI) to hematite in the presence of natural organic matter. *Colloids and Surfaces A Physicochemical and Engineering Aspects*, *157*(1–3), 47–62.

National Stratigraphic Commission of Uganda (2011) Personal communication during workshop and field trip: stratigraphy of the Albertine Graben, Uganda – status. Petroleum Exploration & Production Department of Uganda. July 1, 2011, Lake Victoria Hotel, Entebbe.

Nichols, G.J. (2009) *Sedimentology and stratigraphy*, 2nd edition. New York: Wiley-Blackwell, p. 432.

Parkinson, D.N. (1996) Gamma-ray spectrometry as a tool for stratigraphical interpretation: examples from the western European Lower Jurassic. *Geological Society, London, Special Publications*, *103*(1), 231–255. https://doi.org/10.1144/gsl.sp.1996.103.01.13

Paton, T.R. (1974) Origin and terminology for gilgai in Australia. *Geoderma*, *11*, 221–242.

Peterson, J., MacDonell, M., Haroun, L., Monette, F., Hildebrand, D. & Taboas, A. (2007) Radiological and chemical fact sheets to support health risk analyses for contaminated areas. *Argonne National Laboratory Environmental Science Division*, p. 133.

Petschick R. (2001) MacDiff 4.2.5. http://servermac.geologie.uni-frankfurt.de/Rainer.html.

Petschick, R., Kuhn, G. & Gingele, F. (1996) Clay mineral distribution in surface sediments of the South Atlantic: sources, transport, and relation to oceanography. *Marine Geology*, *130*(3–4), 203–229.

Pickford M., Senut B., & Hadoto, D. (1993) Geology and Palaeobiology of the Albertine Rift Valley Uganda Zaire, Volume I: geology. International Center for Training and Exchanges in the geosciences, Orleans.

Ramón, J.C. & Cross, T. (1997) Characterization and prediction of reservoir architecture and petrophysical properties in Fluvial Channel sandstones, middle Magdalena Basin, Colombia. *CT&F – Ciencia, Tecnología y Futuro*, *1*(3), 19–46. http://www.scielo.org.co/scielo.php?script=sci_arttext&pid=S0122-53831997000100002&lng=en&tlng=en

Rasmussen, C., Reichenbacher, B., Lenz, O., Altner, M., Penk, S.B.R., Prieto, J. & Brüsch, D. (2017) Middle–late Miocene palaeoenvironments, palynological data and a fossil fish Lagerstätte from the Central Kenya rift (East Africa). *Geological Magazine*, *154*(1), 24–56.

Reineck & Singh. (1980) *Depositional sedimentary environments. With teference to terrigenous clastics*. Paris, London: Springer. https://doi.org/10.1007/978-3-642-81498-3

Rider M. (1996) *The geological interpretation of well logs*. Gulf pub. Co 2 sub edition. Houston: Rider-French Consulting Limited, 280 pp.

Rojo, I., Seco, F., Rovira, M., Giménez, J., Cervantes, G., Martí, V. & Pablo, J.d. (2009) Thorium sorption onto magnetite and ferrihydrite in acidic conditions. *Journal of Nuclear Materials*, *385*(2), 474–478.

Roller, S., Hornung, J., Hinderer, M. & Ssemmanda, I. (2010) Middle Miocene to Pleistocene sedimentary record of rift evolution in the southern Albertine graben (Uganda). *International Journal of Earth Sciences*, *99*, 1643–1661.

Rosendahl, B.R., Kilembe, E. & Kaczmarick, K. (1992) Comparison of the Tanganyika, Malawi, Rukwa and Turkana Rift zones from analyses of seismic reflection data. *Tectonophysics*, *213*(1–2), 235–256. https://doi.org/10.1016/0040-1951(92)90261-4

Ruffell, A. & Worden, R. (1999) Palaeoclimate analysis using spectral gamma-ray data from the Aptian (cretaceous) of southern England and southern France. *Palaeoecology, Palaeogeography, Palaeoclimatology*, *154*, 313–325.

Schneider, S., Hornung, J. & Hinderer, M. (2016a) Evolution of the western African rift system reflected in provenance changes of Miocene to Pleistocene syn-rift sediments (Albertine rift, Uganda). *Sedimentary Geology*, *343*, 190–205. https://doi.org/10.1016/j.sedgeo.2016.07.013

Schneider, S. (2019) Paleogeographic and tectonic evolution of the western branch of the east African rift system using multiple provenance methods (Albertine rift, Uganda). Darmstadt, Technische Universität [Dissertation]. http://tuprints.ulb.tu-darmstadt.de/8787.

Schneider, S., Hornung, J. & Hinderer, M. (2017) Evolution of the northern Albertine rift reflected in the provenance of snyrift sediments (Nkondo-Kaiso area, Uganda). *Journal of African Earth Sciences*, *131*, 183–197. https://doi.org/10.1016/j.jafrearsci.2017.04.012

Schneider, S., Hornung, J., Hinderer, M. & Garzanti, E. (2016b) Petrography and geochemistry of Modern River sediments in an equatorial environment (Rwenzori Mountains and Albertine rift, Uganda) – Implications for weathering and provenance. *Sedimentary Geology*, *336*, 106–119. https://doi.org/10.1016/j.sedgeo.2016.02.006

Schnyder, J., Ruffell, A., Deconinck, J.-F. & Baudin, F. (2005) Conjunctive use of spectral gamma-ray logs and clay mineralogy in defining late Jurassic–early cretaceous palaeoclimate change (Dorset, U.K.). *Palaeogeography, Palaeoclimatology, Palaeoecology*, *229*, 303–320.

Simon B. (2015) Rift du Lac Albertine, Ouganda, Rift East Africain: DéFormation, érosion, sédimentation et bilan de matière depuis 17 Ma. PhD thesis, University of Rennes, 403 pp.

Simon, B., Guillocheau, F., Robin, C., Dauteuil, O., Nalpas, T., Pickford, M., Senut, B., Lays, P., Bourges, P. & Bez, M. (2017) The formation and sedimentary evolution of the Lake Albertine rift (Uganda, east African rift system). *Marine and Petroleum Geology*, *86*, 17–37.

Stamps, D.S., Calais, E., Saria, E., Hartnady, C., Nocquet, J.-M., Ebinger, C.J. & Fernandes, R.M. (2008) A kinematic model for the East African Rift. *Geophysical Research Letters*, *35*(5). https://doi.org/10.1029/2007gl032781

Stow, D.A.V., Hernández-Molina, F.J., Llave, E., Sayago-Gil, M., Díaz del Río, V. & Branson, A. (2009) Bedform-velocity matrix: the estimation of bottom current velocity from bedform observations. *Geology*, *37*(4), 327–330. https://doi.org/10.1130/G25259A.1

Talbot, M.R. & Williams, M.A.J. (2009) Cenozoic evolution of the Nile Basin. In: Dumont, H.J. (Ed.) *The Nile: origin, environments, limnology and human use*. Netherlands: Springer, pp. 37–60. https://doi.org/10.1007/978-1-4020-9726-3_3

Taylor, R.G. & Howard, K.W.F. (1998) Post-palaeozoic evolution of weathered landsurfaces in Uganda by tectonically controlled deep weathering and stripping. *Geomorphology*, *25*, 173–192.

Thompson, R., Battarbee, R.W., O'Sullivan, P.E. & Oldfield, F. (1975) Magnetic susceptibility of lake sediments. *Limnology and Oceanography*, *20*, 687–698.

Todd, S.P. (1989) Stream-driven, high-density gravelly traction carpets: possible deposits in the Trabeg Conglomerate Formation, SW Ireland and some theoretical considerations of their origin. *Sedimentology*, *36*(4), 513–530. https://doi.org/10.1111/j.1365-3091.1989.tb02083.x

Turcotte, D.L., & Emerman, S.H. (1983). Mechanisms of active and passive rifting. Developments in geotectonics. In: Morgan, P. and Baker, B.H. (Eds.) *Processes of continental rifting*. *Tectonophysics*, *94*, pp. 39–50. https://doi.org/10.1016/b978-0-444-42198-2.50010-9

Van Damme, D. & Pickford, M. (2003) The late Cenozoic Thiaridae (Mollusca, Gastropoda, Cerithioidea) of the Albertine Rift Valley (Uganda-Congo) and their bearing on the origin and evolution of the Tanganyikan thalassoid malaco fauna. *Hydrobiologia*, *498*, 1–83.

Vasconcelos, P.M., Brimhall, G.H., Becker, T.A. & Renne, P.R. (1993) 40Ar/39Ar analysis of supergene jarosite and alunite: implications to the paleoweathering history of the western USA and West Africa. *Geochimica et Cosmochimica Acta*, *58*, 401–420.

Viers, J., Dupré, B., Polvé, M., Schott, J., Dandurand, J.-L. & Braun, J.-J. (1997) Chemical weathering in the drainage basin of a tropical watershed (Nsimi-Zoetele site, Cameroon): comparison between organic-poor and organic-rich waters. *Chemical Geology*, *140*(1997), 181–206.

WoldeGabriel, G., Aronson, J. & Walter, R. (2000) Volcanism, tectonism, sedimentation, and the palaeoanthropological record in the Ethiopian rift system. *Geological Society of America Special Paper*, *345*, 83–99.

SUPPORTING INFORMATION

Additional supporting information can be found online in the Supporting Information section at the end of this article.

How to cite this article: Hornung, J., Hinderer, M., Brüsch, D. & Petschick, R. (2023). An exceptional sedimentary record of initial rifting on the East African Plateau in the Miocene: Lessons from depositional cyclicity and palaeoenvironmental proxies. *The Depositional Record*, *9*, 52–82. https://doi.org/10.1002/dep2.207